# Coastal Trapped Waves and other subinertial variability along the Southeast Greenland Coast in a realistic numerical simulation

Renske Gelderloos*, Thomas W. N. Haine, and Mattia Almansi†

*Department of Earth and Planetary Sciences, The Johns Hopkins University, Baltimore, MD*

**Corresponding author*: Renske Gelderloos, rgelder2@jhu.edu

†Current affiliation: National Oceanography Centre, Southampton, UK

## ABSTRACT

Ocean currents along the Southeast Greenland Coast play an important role in the climate system. They carry dense water over the Denmark Strait sill, fresh water from the Arctic and the Greenland Ice Sheet into the subpolar ocean, and warm Atlantic water into Greenland's fjords, where it can interact with outlet glaciers. Observational evidence from moorings shows that the circulation in this region displays substantial subinertial variability (typically with periods of several days). For the dense water flowing over the Denmark Strait sill, this variability augments the time-mean transport. It has been suggested that the subinertial variability found in observations is associated with Coastal Trapped Waves, whose properties depend on bathymetry, stratification, and the mean flow. Here, we use the output of a high-resolution realistic simulation to diagnose and characterize subinertial variability in sea surface height and velocity along the coast. The results show that the subinertial signals are coherent over hundreds of kilometers along the shelf. We find Coastal Trapped Waves on the shelf and along the shelf break in two subinertial frequency bands—at periods of 1–3 days and 5–18 days—that are consistent with a combination of Mode I waves and higher modes. Furthermore, we find that northeasterly barrier winds may trigger the 5–18 day shelf waves, whereas the 1–3 day variability is linked to high wind speeds over Sermilik Deep.

## 1. Introduction

The Southeast Greenland shelf-slope region harbors several processes that are important for the climate system. Dense water spills over the relatively shallow sill in the Denmark Strait, feeding the lower limb of the Atlantic Meridional Overturning Circulation (AMOC); warm Atlantic water spills into the Greenlandic fjords and interacts with the ice sheet's outlet glaciers. Observations show that both processes display substantial subinertial variability—that is, variations with a time scale of several days. The primary focus of research on the regional circulation in this region has been on long-term mean quantities; but, evidence suggests that subinertial variability affects the mean state significantly: Boluses and pulses increase the dense overflow transport in the Denmark Strait by 30% (Almansi et al. 2017), and warm Atlantic water enters the fjords in this region at quasi-periodic time intervals (Jackson et al. 2014, 2018). Subinertial variability along the shelfbreak could also play an important role in shelf-basin exchange by providing a possible driving mechanism for downwelling along the shelf, which is where the net sinking in the AMOC takes place (Katsman et al. 2018). Understanding and quantifying the processes associated with subinertial variability is thus essential for understanding the mean flow.

Several studies have found subinertial variability in this region. The most well-known source of subinertial variability is the Denmark Strait Overflow, which produces coherent eddies ("DSO eddies") that move dense water downstream from the sill (Jochumsen et al. 2017; Almansi et al. 2017, 2020), and have an imprint on the sea surface temperature (Bruce 1995). Subinertial variability also occurs at the shelf break and on the shelf (von Appen et al. 2014a; Harden and Pickart 2018), and in fjord-shelf exchange flows (Jackson et al. 2014, 2018; Fraser and Inall 2018; Fraser et al. 2018; Spall and Pedlosky 2018). The subinertial variations in observations have shown some coherence between moorings at different along-shelf locations, sparking the

hypothesis that this variability could be associated with Coastal Trapped Waves (CTWs; Harden et al. 2014b; Jochumsen et al. 2017). The small dynamical length scales at high latitudes and the rapid variations in along-shelf bathymetry and the presence of fjords make observing these phenomena challenging. Using a realistic high-resolution model, however, enables us to identify and categorize a variety of subinertial oscillations as well as their spatial structure. This work will help to put *in situ* observations into a wider spatial and temporal perspective and lay the ground work for a further dynamical understanding of these phenomena.

The field of CTWs goes back to early work by Robinson (1964) (though work on internal Kelvin waves predates that paper), who aimed to find an explanation for the deviation of sea surface height variations from the inverse barometer effect in measurements by Hamon (1962, 1963) on the Australian continental shelf. In the next decades, studies expanded on this work by considering the combined effects of sloping bathymetry and stratification in both free and forced wave problems from a theoretical perspective (Mysak 1967b,a; Buchwald and Adams 1968; Adams and Buchwald 1969; Rhines 1970), lab experiments (Caldwell et al. 1972) and *in situ* observations (Mooers and Smith 1968; Cutchin and Smith 1973; Clarke 1977). The term "Coastal Trapped Waves"—a hybrid between barotropic Continental Shelf Waves which are impacted by bathymetry (the ones studied by Robinson (1964)), and internal Kelvin Waves which are impacted by stratification—first appears in Gill and Clarke (1974). Reviews on the topic can be found in Mysak (1980); Huthnance (1978); Brink (2006).

More recently, research on CTWs has benefited from more observational evidence (Inall et al. 2015) and more realistic simulations (Fraser and Inall 2018; Fraser et al. 2018). Observational evidence for subinertial variability is plentiful on the East Greenland shelf and slope (e.g., von Appen et al. 2014a; Harden et al. 2014a,b; Jackson et al. 2014; Fischer et al. 2015; Harden et al.

2016; Harden and Pickart 2018; Bras et al. 2018; Pacini et al. 2020). However, the characteristics of this variability and its relationship to CTWs are still open questions.

The objectives of this manuscript are thus to show that (i) subinertial variability along the Southeast Greenland Coast is coherent along and across the continental shelf, and that (ii) the characteristics of this variability are consistent with CTWs. We find that the signal around the Denmark Strait deviates from the signals found upstream and downstream of the sill. The behavior at the sill indicates nonlinear steepening of propagating waves and interaction with waves propagating around Iceland. Although this behavior is interesting and should be studied, it is beyond the scope of this manuscript. Our focus is on investigating coherence between signals upstream and downstream of the sill region.

This manuscript is structured as follows: Section 2 contains a brief description of the setup of the numerical model used in this study, and some time mean quantities are discussed in Section 3. In Section 4 subinertial variability is diagnosed and characterized, shown to be coherent along the Southeast Greenland Coast, and shown be associated with CTWs. Section 5 shows that some of the variability is forced by wind events. Conclusions from this work are presented in Section 6.

## 2. Numerical model

We use a high-resolution regional ocean-sea ice configuration of the primitive-equation Massachusetts Institute of Technology General Circulation Model (MITgcm; Marshall et al. 1997). The setup is identical to the one used by Almansi et al. (2020), and was not specifically designed to study waves. The main characteristics of the setup are summarized below; for details the reader is referred to Almansi et al. (2017, 2020). For extraction of model fields on hydrographic sections, along mooring arrays, and along isobaths we use the open-source software package OceanSpy (Almansi et al. 2019), and for the data analysis we use jLab (Lilly 2019).

The model domain is centered around the Denmark Strait and includes the southeast Greenland shelf region, the entire Greenland-Scotland Ridge, the Irminger and Iceland Seas, the Iceland Basin, and parts of the Greenland and Norwegian Basins (Figure 1). The model is run in hydrostatic mode with 216 vertical levels, ranging from 2 m at the surface to 15 m below 120 m depth. The horizontal resolution is 2 km around the Denmark Strait, decreasing to 4 km near the boundaries of the domain. The model was run for 1 year from September 2007 to August 2008, after an initial 8 month spinup as described by Almansi et al. (2017), and snapshots of the fields were stored every 6 hours. At the open boundaries, tracer values and velocities are nudged towards daily HYCOM+NCODA 1/12° global reanalysis fields (Cummings and Smedstad 2013). Sea surface temperatures are relaxed to the Operational Sea Surface Temperature and Sea Ice Analysis (OSTIA) global product (Donlon et al. 2012), and atmospheric forcing is provided by the 3-hourly 15-km Arctic System Reanalysis (ASRv2; Bromwich et al. 2018). The boundary and surface forcing field are linearly interpolated in time by the MITgcm before they are applied. This model setup has no tidal forcing.

The ocean model is coupled to a viscous plastic dynamic/thermodynamic sea ice model (Losch et al. 2010; Heimbach et al. 2010) with the subgrid-scale salt plume parameterization (Nguyen et al. 2009). Sea ice values are nudged over 20 grid points from the open boundaries to the monthly 1/8° Towards an Operational Prediction System for the North Atlantic European Coastal Zone reanalysis, version 4 (TOPAZv4; Sakov et al. 2012). Freshwater forcing from the Greenland ice sheet is based on Noël et al. (2016) for surface runoff and Bamber et al. (2012) for solid-ice discharge.

## 3. Mean flow and stratification along the shelf in the numerical model

This model setup and previous versions of the same setup have been shown to realistically simulate the ocean circulation in the greater Denmark Strait region (Haine 2010; Magaldi et al.

2011; Koszalka et al. 2013; von Appen et al. 2014b; Gelderloos et al. 2017; Almansi et al. 2017; Håvik et al. 2019; Almansi et al. 2020; Saberi et al. 2020; Foukal et al. 2020). We focus here on the time-mean current and density fields (the mean SSH has no impact on wave dynamics, unlike the mean flow and stratification and is therefore not discussed; note that SSH variability, on the other hand, is crucial and will be discussed in the next section) at 11 roughly equally-spaced stations along the 200-m isobath and at 11 stations also roughly equally spread out along the 450-m isobath (red and blue stars in Fig. 1, respectively); The 200-m isobath (green contour in Fig. 1) hugs the coast, while the 450-m isobath (magenta contour in Fig. 1) roughly delineates the shelf break along the Southeast Greenland coast within the model domain.

Before looking at the velocity structure along the coast, we compare the velocity across a single section at the Kögur line (magenta line in Fig. 2c) with available observations. Fig. 2a shows the velocity from a gridded product based on moored instrument measurements in 2011-2012 (Harden et al. 2016), and panel (b) shows its model counterpart. The model captures the magnitude and location of the shelfbreak current maximum (around 20 km) well. The model core is wider than in observations, but the Greenland shelf was sparsely sampled by the moorings and the agreement on the shelf is still very good compared to densely sampled hydrographic surveys (see Fig. 2 in Foukal et al. 2020). The mean velocity vectors for the 22 coastal and shelf break stations are plotted for three depth ranges in Fig. 2c. The mean flow at all stations is along the coast in a southwesterly direction, consistent with observations. The large mean velocities along the shelf break are due to the shelfbreak jet called the East Greenland Current (Rudels et al. 2002; Håvik et al. 2017). Closer to the coast the mean velocities are smaller, with most stations being in the East Greenland Coastal Current (Bacon et al. 2002; Foukal et al. 2020; Håvik et al. 2017). Except for stations 5–7 on the 450-m isobath (i.e., immediate south of the Denmark Strait sill), the current is surface intensified and decreases monotonically with depth. South of the Denmark Strait sill,

the deep flow (in the overflow plume) is stronger than the currents at middepth and at station 5 even than the near-surface currents; the deep flow backs with respect to the surface currents (i.e., is directed in a more southerly direction than the current near the surface), which is in line with observations (Harden et al. 2014a).

Fig. 3 shows the vertical density structure for the stations on the 200-m (450-m) isobath in panel a (b). All stations show stronger stratification near the surface. This is especially true in summer, when solar heating and melting ice add buoyancy to the surface layers. In winter, storms, brine rejection from freezing, and intense ocean heat loss erode the summertime stratification. The model is biased somewhat fresh in the upper ocean (Almansi et al. 2017; Saberi et al. 2020), and is therefore more stratified than observations (compare the contours in panels (a) and (b) of Fig. 2). As will be shown in Section 4d, differences in stratification have only a minor impact on the wave properties.

## 4. Characteristics of subinertial variability in the numerical model

Subinertial variability is manifested in variations about the mean conditions laid out in Section 3. This variability can be substantial: on the shelf, it can temporarily change the transport direction of the mean current (Foukal et al. 2020), which is important to keep in mind when working with synoptic surveys. We explore this variability with respect to mean conditions in sea surface height and current velocity.

### *a. Subinertial variability in sea surface height*

Model sea surface height time series are extracted at the 22 coastal and shelf break stations. The time series are detrended, have their time means subtracted and a multitaper is applied to reduce broadband bias and spectral variance (Thomson 1982; Lilly 2019). The resulting spectral estimates

are plotted in Fig. 4a. For reference the spectral estimates from the Ammassalik and the Qaqortoq tide gauges from hourly data over 1994–1995 are shown in Fig. 4b. The tide gauge records were first low-pass filtered using a 10th order Butterworth filter with a cutoff frequency of 1.3 days, subsequently detided using T-TIDE (Pawlowicz et al. 2002) to remove any lower frequency variability associated with tides.

Several maxima in the subinertial frequency range (left of the vertical gray dashed line) are found: First, two near-inertial peaks (0.5–0.6 days at 0.6–0.7 days) are evident in all 200-m and 450-m stations, indicating that there exists high-frequency variability with similar spectral behavior across the entire shelf in the model. These peaks lie between the diurnal and the semi-diurnal tidal frequencies, and are absent from the tide gauge records (even before low-pass filtering). We have carefully investigated this variability, and conclude that they represent spurious variability in the form of a seiche about the Greenland-Iceland-Scotland Ridge, probably arising as a resonance in response to discontinuities in the boundary forcing (which is piecewise linear in time after interpolation). To make sure the presence of this high frequency variability has no major impact on our results, the low-pass filtering procedure for the tide gauge record has also been applied to the model SSH time series in the remainder of the results shown.

Second, there is a broad spectral peak at almost all stations around 1.3–2.8 days (hereafter referred to as 1–3 days), with a single outlier at station 5 along the 450-m isobath (just downstream of the Denmark Strait sill), which has its peak at slightly higher frequency (1.0–2.2 days), with much larger spectral power. The tide gauge records show elevated energy levels between 1 and 3 days as well, though perhaps split in two peaks (1–2 days and 2–4 days). The Qaqortoq station in particular exhibits a sharp peak in the 1–2 day range. Third, there is a less distinct broad maximum around 10 days found at all model stations. The tide gauge record at Ammassalik shows several

peaks in this frequency range including a relatively narrow peak around 10 days; the Qaqortoq record exhibits a broad peak more like the model records.

The similarities between the various curves in Fig. 4a are a strong indication of coherent variability. This coherence is now quantified by calculating the complex coherence between two time series, $x$ and $y$, as

$$\gamma = \frac{S_{xy}}{\sqrt{S_{xx}S_{yy}}}, \tag{1}$$

where $S_{xy}$ is the cross spectrum of $x$ and $y$, and $S_{xx}$ and $S_{yy}$ are the one-sided spectra of $x$ and $y$, respectively. The magnitude of the complex coherence is a value between 0 and 1, where 0 means no correlation and 1 means the two time series are perfectly coherent at that frequency. The phase angle of the complex coherence is a measure of the phase lag between the time series, which may include multiples of $2\pi$. We calculated the coherence for all station pairs on the 200-m isobath and all pairs on the 450-m isobath, and averaged the coherence magnitude and phase over the two frequency ranges identified from Fig. 4; the mean phase was calculated as the circular mean according to Grinsted et al. (2004).

The results for the coherence with station 1 on both isobaths is shown in Fig. 5. The coherence at 0 km is naturally 1 at 0 phase lag (the coherence of the time series with itself). The coherence (panels a,b) drops with distance along the coastline. Along the 200 m isobath (Fig. 5a), coherence in the 1–3 day signal drops faster than in the 5–18 day signal; the reverse is true for the 450 m isobath (Fig. 5b), where coherence between stations is stronger in the 1–3 day band. The same holds when coherence with a different station than station 1 is plotted (not shown). The phase lags (panel c,d) show different behavior too between the two isobaths: Along the 200 m isobath (Fig. 5c), the phase gradually changes from 0 to $\pi/2$ along the length of the shelf. The change is more gradual for the 5–18 day curve than for the 1–3 curve, which would be consistent with a longer-wavelength propagating signal in the 5–18 day band than in the 1–3 day band. Along the

450 m isobath (Fig. 5d), the phase difference is small up to station 4, and then suddenly shifts across the Denmark Strait sill. This is particularly evident in the 1–3 day curve, as the 5–18 curve exhibits a large uncertainty at station 4.

Another way to visualize coherence along and across the continental shelf is with a wavelet analysis (Torrence and Compo 1998). We calculate the energy contained in the two frequency bands above using a continuous Morlet wavelet transform $\left(\Psi_0(\eta) = \pi^{-1/4} e^{i\omega_0\eta} e^{-\eta^2/2}\right)$ with non-dimensional frequency $\omega_0 = 6$, which is a common choice for feature extraction as it provides a good balance between time and frequency localization (Grinsted et al. 2004); $\eta$ is the dimensionless time. This procedure yields a time series of wavelet energy per frequency band for every station analyzed. The results (Fig. 6) show pulses of energy (note that individual peaks in Fig. 6 are not waves, but an elevated level of energy in that frequency band at that location), which in some cases persist over several stations. The blue peak in early February 2008, for example, can be traced all the way from station 1 to station 11. The red peaks in the first half of the station 7 record, on the other hand, seem to start at station 6, grow in amplitude, and die out after station 9. Some events (especially for the 1–3 day curves around Denmark Strait) are even local to only one station.

Both analyses presented above show strong evidence for spatially coherent variability, but we can go a step further: One of the major advantages of analyzing model data is that the full 4D fields are available for analysis. We will now determine the spatial patterns that accompany the signals found above. To this end, the sea surface height anomaly time series of every grid point in the entire model domain is individually band-pass filtered for two pass bands based on the maxima identified in Fig. 4. We used a 5th order Butterworth filter and passed the filter forwards and backwards to avoid phase shifting of the signals. Animations of the time-evolving fields are provided as supplementary material to this manuscript; Fig. 7 shows snapshots selected to highlight certain features.

Fig. 7a-c are examples of the 1–3 day band-pass filtered fields. Panel (a) exhibits a traveling wave on the Greenland continental shelf, spanning the width of the shelf, and propagating with the coast on the right hand side. This is characteristic for Continental Shelf Waves (purely barotropic CTWs). A traveling wave around Iceland of a single wavelength is also evident in the 1–3 day (as well as the 5–18 day) band-pass filtered fields, and less obvious but still present are waves along the Greenland-Iceland-Scotland Ridge and along Reykjanes Ridge (the red blob southwest of Iceland). The inset in panel (b) and panel (b) itself show the merging of a wave traveling in northeasterly direction around Iceland (in clockwise direction, with the coast on the right hand side) and a wave of similar wavelength traveling southwestward along the Greenland shelf, also with the coast on the right hand side (note that these are snapshots from two different events, but they are representative for this phenomenon as can be seen in the animation). The two waves phase lock at the Denmark Strait sill and appear to energize the wave traveling along the Greenland coast, which is consistent with the much larger spectral peak at station 5 compared to other stations (Fig. 4a). Panels (b) and (c) both show traveling waves of a much shorter wavelength than the one in panel (a), predominantly along the shelf break upstream of the Denmark Strait sill (panel b) and predominantly on the shelf along the coastline starting at Sermilik Deep (panel c). The latter pathway has been documented from mooring observations by Harden et al. (2014b). Fig. 7d-f are examples of the 5–18 day band-pass filtered fields, which show similar features as the 1–3 day filtered fields but with larger wavelengths: This frequency band also exhibits a fast traveling wave along the continental shelf (panel d) which in this case spans almost the entire length of the shelf in the model domain for half a wavelength. Panel (e) and (f) shows the shorter-wavelength slower moving wave on the shelf break, with a larger wavelength than in the 1–3 day frequency band.

In summary, spectral peaks in the SSH anomaly time series are found around 1–3 days and a broad peak around 10 days. The signals show strong coherence along and across the shelf. There

are two types of spatial patterns in the band-passed filtered fields associated with these frequency bands: First, a fast moving wave spanning the width of the continental shelf that travels with the coast on the right hand side. This type of wave is present in both frequency bands, and has a larger wavelength in the lower frequency range. Second, slow-moving short-wavelength waves are found along the shelfbreak and on the shelf near the coastline. These waves are also longer in the 5–18 bands compared to the 1–3 days band. Upstream of and in the Denmark Strait, these waves are most prominent along the shelf break; from Sermilik Deep onward the coastal wave has a larger amplitude.

*b. Subinertial variability in velocity fluctuations*

Current velocity can also shed light on subinertial variability. Unlike SSH, current fluctuations contain information on vertical structure of the variability. Furthermore, if the subinertial variability is a signature of waves, we expect to find a consistent relationship between the SSH anomalies and the current fluctuations in the frequency range in question (See Section 4c). In this section we focus on the velocity fluctuations.

Velocity variance ellipses indicate the magnitude and preferred direction of current variations with respect to the mean flow. Fig. 8 shows the variance ellipses of the velocity fluctuations at the 22 coastal and shelf break stations. The ellipses are drawn for all model depth levels in the water column; color coding is by depth, with light colors near the surface. The ellipses portray behavior that is characteristic for boundary current variability: the ellipses are more elongated and aligned with the bathymetry at depth compared to the surface, as the solid boundaries constrain lateral current fluctuations. The magnitude of the fluctuations also decreases with depth as bottom friction becomes more important. Although the stations share many similarities, the shelf stations downstream of Denmark Strait have larger current fluctuations than the shelf stations upstream of

Denmark Strait (Fig. 8a). This is consistent with the observation in Section 4a that the short-wavelength traveling waves are more prominent on the shelf in the Irminger Sea. The shelfbreak station directly downstream of the Denmark Strait sill (station 5) portrays different behavior from other stations: the ellipses are near circular, and increase rather than decrease in size with depth. The velocity fluctuations at this station are thus dominated by bottom-intensified eddies, as expected for a station in the path of the DSO eddies.

The variance ellipses indicate that the preferred direction of the current variability is alongshore. They do not give information on the frequency ranges that variability is manifested in (the current ellipses of band-pass filtered velocity time series are only qualitatively different at station 5 on the 450 m isobath for the 5-18 day frequency range, where the DSO eddy signal is no longer evident). We thus calculate the rotary spectra of the current fluctuations. For example, Fig. 9 shows the cyclonic and anticyclonic spectra at 100 m depth of station 4 along the 200-m and the 450-m isobaths. Inertial oscillations on the shelf are clear in Fig. 9 as there is a broad peak around the inertial frequency in the anticyclonic side of the spectrum (solid black curve) only, which is consistent with inertial oscillations in the Northern Hemisphere. Inertial oscillations are evident in stations 2–6 on the 200-m isobath (not shown), but none of the 450-m isobath stations exhibit this feature. In general, the 200-m isobath station spectra are more consistent with each other than the 450 m isobath station spectra.

The peaks in the SSH spectra are indicated in Fig. 9 using whiskers with the same colors as Fig. 4. In the 1–3 day range, there are 1 or sometimes 2 peaks in the velocity spectra. On the 200 m isobath, the energy in the anticyclonic component consistently exceeds the energy in the cyclonic component, though maxima are evident in both spectra. On the 450 m isobath, the 1–3 day peaks are present in the stations upstream of the Denmark Strait and downstream of it the peak has shifted to 2–4 days (not shown). The 5–18 day peak is visible as a weak and broad maximum at most

stations. At the 450 m isobath stations, the peak is somewhat narrower than in the SSH anomaly spectra and confined to roughly 5–12 days.

### *c. Wave properties*

The evidence in Section 4a shows that waves exist in the sea surface height field in the subinertial frequency range, propagating with the coast on the right hand side. This is physically consistent with CTWs in the Northern Hemisphere. In this section we analyze the properties of the waves found in the model fields.

Figs. 10 and 11 show Hovmöller diagrams of the SSH signals on the 200 m and the 450 m isobaths, respectively, bandpass filtered over 1–3 days (panels a) and 5–18 days (panels b). A limited time frame is displayed to highlight the propagating signals. Fig. 10 is dominated by near-horizontal stripes: these are barotropic waves that propagate at a speed of 100s of kilometers per day. The entire length of the shelf (about 2000 km) fits two waves in the 1–3 days band and half a wave in the 5–18 day band, which gives wavelengths of 1000 km and 4000 km, respectively. Slower propagating signals are present too, for example starting at the entrance of Sermilik Deep (at a distance of 2500 km in Fig. 10). Recall from Fig. 7 that the slower waves upstream mostly manifest along the shelfbreak (see also Fig. 11). The phase speed of the short waves on the shelf as derived from the slope of the lime green lines is roughly 0.5 m $s^{-1}$ in the 1–3 day band and slightly faster in the 5–18 day band—twice as fast as the mean flow. Along the shelf break (Fig. 11) short waves with a wavelength of 40 km propagate in the 1–3 day band with a phase speed of 0.38 m $s^{-1}$ in the Blosseville Basin (directly upstream of station 4). Along the same stretch in the 5–18 day fields the waves are 200 km long and the phase speed is 0.19 m $s^{-1}$. Still, these waves move faster than the mean flow by factors of 4 and 2, respectively. At the Denmark Strait sill (between stations 4 and 5) the two frequency bands behave differently. The waves in the 5–18

day band continue as before, but the waves in the 1–3 day band accelerate over the sill with a mean speed of 2.72 m $s^{-1}$ and grow in amplitude. Downstream of the sill, the phase speeds of the waves in the two frequency bands are the same at 0.44 m $s^{-1}$, which is slightly higher than the upstream value in the 1–3 day band and much faster than in the 5–18 day band. It is surprising that we find the same phase speeds in these two frequency bands because the properties differ elsewhere along the shelf. The wavelength in the 1–3 (5–18) day band is 80 (200) km. The waves are particularly evident where the shelf is narrow (in the Irminger Sea). These are the same waves as the ones in Fig. 10a because the 200 and 450 m isobaths are close together at this stretch of coastline (see Fig. 7d and also the supplementary animations).

### *d. Comparison to theory*

We compare the model waves to CTW solutions from theory in this section. The theoretical solutions cannot fully account for both strong alongshore mean flow (e.g., Niiler and Mysak 1971; Mysak 1980) and strong along-shore and cross-shore changes in bathymetry (e.g., Johnson and Clarke 2001; Rodney and Johnson 2012, 2014, 2015). We therefore choose a model section that is upstream of the largest bathymetric changes (cyan line in Fig. 1), where the theory is least erroneous. We compute CTW solution modes using the iterative method of Brink (1982, 2006), which accounts for a (steady, surface intensified) mean flow. Details of the procedure can be found in the manual (Brink 2018); in essence, the algorithm solves a partial differential equation for the pressure field iteratively to find a valid combination of pressure, wave frequency, and along-shore wave number, given a bathymetric profile, a density field, Coriolis frequency, mean flow structure and speed, top and bottom boundary conditions for surface and bottom stress, and open or closed side boundary conditions. The bathymetry on our section is approximated (following Dale et al. (2001); Inall et al. (2015)) by a flat 80 km wide and 300 m deep shelf, a 40 km wide continental

slope, and a flat 80 km wide ocean floor at 1650 m depth, which represents the cross shelf profile well (Fig. 12b). At the offshore edge of the domain an open boundary condition is applied. For the stratification, the mean summer and winter profiles from Fig. 3 are used. The Brink (1982, 2006) method is known to fail to find solutions when the spatial scale of the wave is much smaller than the domain width. Indeed, we cannot find stable solutions for very short waves or modes higher than II.

The dispersion relations for the first two CTW modes are plotted in Fig. 12a. We consider several cases for summer and winter stratification and surface-intensified mean flows between 0.1 and 0.4 m $s^{-1}$. In all cases the stratification differences are unimportant. The solutions are sensitive to the mean flow for wavelengths less than about 300 km. In these cases, stronger mean flow increases the wave frequency and thus the phase speed at fixed wave number. The effect is most pronounced in the Mode I solutions. Variations in the strength of the mean flow have little impact on the cross-shore spatial structure of the wave solutions. The bathymetry has a significant impact on the wave solutions, but a detailed exploration of its effect is unnecessary for the goals of this paper.

The three wave solutions diagnosed from the model fields that fall within the $\omega$–$k$ range of Fig. 12a are indicated by the connected open circles. The long fast waves on the shelf (both 1–3 days and 5–18 days) are in the lower left corner and are consistent with the Mode I theory. The shorter 5–18 day waves at the shelfbreak fall at lower frequencies than the Mode II theoretical curve. Based on their low phase speed and (cross-shelf) spatial structure, we hypothesize that these waves are Mode III waves, which the Brink (2006) algorithm fails to identify. A hypothetical Mode III curve is added to the dispersion diagram as a gray dashed line, based on expectations from the literature (e.g. Caldwell et al. 1972). The presence of a Mode III wave on the shelf break is supported by evidence from Pacini et al. (2020), who found this mode at the shelf break in southwest Greenland.

To compare the cross-shore spatial structure of the model waves with the CTW theory we perform a multivariate Empirical Orthogonal Functions (MEOF) analysis on the model SSH and surface velocity fields along the same cyan line in Fig. 1 that was used to find the theoretical solutions (we performed the analysis also with band-pass filtered fields, which yielded very similar results). The purpose of this MEOF analysis is to find coupled variability structures between the different (model) variables that are associated with CTWs, so that they can be directly compared to the theoretical solutions. Before calculating the MEOFs, we remove the time mean from each model field and normalize them with their global standard deviation. This ensures equal contribution of all fields to the MEOF variance analysis (Wheeler and Hendon 2004). All MEOFs presented here are independent based on North's criterion (North et al. 1982). MEOFs I and II have no zero-crossing in SSH and therefore do not resemble CTWs. Fig. 12c-e show MEOFs III–V which explain 14%, 9%, and 6% of the total combined variance, respectively.

In panel (a) four examples of theoretical CTW wave structures are plotted (insets A-D), to be compared to the MEOF structures. In general, variance is maximized closer to the coast line for low wave numbers (A and B), and in the shelf break region for higher wave numbers (C and D). At low wave numbers, the along-shelf velocity (red curve) is at a uniform maximum across the shelf; at higher wave numbers the maximum is instead mid-shelf with a slight reduction in amplitude toward the coast. The pressure (blue curves) is maximum at the coast in the mode I cases (A and C), while it is zero at the coast for mode II (B and D). Cross-shore velocity (green curves), finally, is zero at the coast for both mode I and mode II waves, increases in magnitude to a maximum mid-shelf, and then decreases. Although the model MEOF structures are noisy, especially close to the coast where the model fields are impacted by more complicated bathymetry (Fig. 12b), they are remarkably similar to the CTW modes in panel (a). In particular, MEOF III (panel c) has a maximum SSH at the coast and a mid-shelf maximum for along-shelf velocity. This would be

consistent with a mode I wave of moderate to high wave number. MEOF IV (panel d) has zero SSH anomaly at the coast and a broad maximum along-shelf velocity (only going to zero very close to the coast). This is consistent with the structures found in mode II waves in panel (a). MEOF V (panel e), finally, is inconclusive as it shows features of both mode I and mode II waves, but is also a lot more noisy (particularly in along-shore velocity) than MOEFs III and IV. Overall, the variability in the 1–3 days and 5–18 days bands in the MITgcm model solution are consistent with CTWs.

## 5. The role of wind in driving subinertial variability

We have shown the presence of subinertial variability in several of the model fields, the frequency bands in which they are manifested, their spatial structures, and that the model variability in these frequency bands exhibit behavior that is consistent with the known properties of CTWs. This naturally leads to the question what drives this variability. One of the driving forces often suggested in the literature is wind—in particular strong alongshore winds (e.g., Harden et al. 2014b; Inall et al. 2015). To investigate the possible role of wind, we perform an MEOF analysis on the combinations of ASRv2 wind speed fields and bandpass-filtered SSH anomaly fields.

Fig. 13 shows an example of the results from the MEOF analyses (chosen because it highlights the signature of shelf waves). Panels (a) and (b) show the 2nd EOFs for SSH anomaly and wind speed, respectively. This EOF explains 9% of the total variance in the two combined fields; the 1st EOF (not shown) is mostly a signature of the seasonal cycle in wind speed and contains 14% of the total variance. The most striking feature in Fig. 13a is the elevated positive (note that the sign is arbitrary) band along the Greenland shelf, combined with peaks and troughs spanning the width of the shelf within this band of high positive values. This physically corresponds to a Continental Shelf Wave (spanning the entire length of the shelf at this frequency, Fig. 7d) with shorter waves

superimposed. The corresponding wind EOF resembles a barrier wind (Petersen et al. 2009). (Figure 13c shows that the barrier wind pattern found in the MEOF analysis is very similar to the 3rd EOF of wind speed only, explaining 7% of the variance in the fields of this variable.) The amplitude of the second (shared) principle component that accompanies both MEOF fields in panels (a,b) is shown as the blue curve in Fig. 13d. Consecutive sharp maxima correspond to peaks and troughs in the phase of a Continental Shelf Wave in this frequency band, as illustrated in panels (e-h). The green curve in panel (d) illustrates a partial correspondence between local elevated levels of wavelet energy and periods of large amplitude peaks in the second principle component.

The evidence in Fig. 13 is inconclusive, but indicates that at least part of the variability in the 5–18 day frequency band is forced by barrier winds. Performing the same analysis on the 1–3 day bandpass filtered fields shows that variability in this frequency band is also partially wind driven. In this case the wind speed maximum is further south over Sermilik Deep (see also Harden et al. (2014b)). This pattern corresponds to the 2nd EOF of wind speed alone. So, the 2nd and 3rd wind speed EOFs (not MEOFs) are associated with SSH variability in the 1–3 day and the 5–18 day frequency bands, respectively. Not all variability in these frequency bands is linked to wind forcing, however.

## 6. Summary and Discussion

The goals of this study are to show that (i) subinertial variability along the Southeast Greenland Coast is coherent along and across the continental shelf, and (ii) the frequency bands of this variability and their spatial structures are consistent with CTWs. We use output from a realistic high-resolution numerical simulation to diagnose and characterize subinertial variability in the flow field with a focus on SSH anomalies and velocity fluctuations.

We find two subinertial bands in the frequency spectrum of SSH anomaly time series, at 1–3 and at 5–18 days. Using statistical coherence and visual inspection of the time-varying SSH fields, we show that much of this variability is spatially coherent. In particular, we find two types of waves: (i) long-wavelength (1000-4000 km) fast-propagating (100s–1000s of km/day) waves on the continental shelf that span the width of the shelf, and (ii) short-wavelength (10s-100s km) slowly propagating (0.1-0.5 m $s^{-1}$) waves along the shelf break upstream of Sermilik Deep and along the coast downstream of Sermilik Deep.

CTW properties from theory are consistent with the subinertial variability in the model. The fast, long waves in the 1–3 and 5–18 days bands are consistent with a Mode I wave. The short waves along the shelfbreak in the 5–18 day band are likely Mode III waves. We are unable to ascertain that the shelf-break wave in the 1–3 day range is a CTW, but the structure (Fig. 7b,c) and propagation (Fig. 11a) are consistent with CTWs. The 5–18 day fast shelf waves are sometimes associated with barrier wind events, whereas the 1–3 day waves are sometimes associated with strong northeasterly winds over Sermilik Deep.

The variability around the Denmark Strait sill differs from the variability elsewhere. In the 1–3 day band in particular, the waves accelerate and grow in amplitude as they approach the sill, morph temporarily into coherent eddies, and return to wavelike characteristics downstream of the Denmark Strait sill. Boluses and pulses at the Denmark Strait sill are possibly associated with this steepening, as the extreme phase speed acceleration promotes nonlinearities. The phase-locking behavior at the Denmark Strait sill of waves traveling southwards along the Greenland coast with waves propagating northwards around Iceland (Fig. 7b) is reminiscent of the flooding events described by Spall et al. (2019) in the way the flooding events are associated with an intense meandering of the hydrographic front. The phase locking phenomenon provides a way to energize and possibly destabilize the frontal currents. The phase-locking occurrence frequency is however

much higher than once a month; it is possible that the flooding event is one possible manifestation of this phase-locking phenomenon.

While this study has shown that CTWs are indeed a prominent feature of the ocean dynamics along the Southeast Greenland coast, many open questions remain. For example, wave motion around Iceland appears to be intricately linked to wave motion along the Southeast Greenland coast, and the two together appear to determine wave propagation in the Denmark Strait. Wave dynamics around Iceland are particularly interesting as the allowable wavelengths are set by the circumference of the island. Characterizing and understanding wave dynamics around Iceland is thus crucial to understanding subinertial variability in the Denmark Strait, and this will be discussed in a follow-up manuscript. A second largely open question is what drives the subinertial variability, and in particular whether the waves are forced locally or remotely. We have shown that local wind events can account for some of the variability, but not all of it, indicating at least some waves are likely forced remotely and brought in through the open boundaries. This question is left for a future paper. A third area that is largely unexplored in this manuscript is the impact of along-shelf variations in bathymetry on wave properties. Emergent theoretical work on this topic (e.g. Rodney and Johnson 2014) shows a rich behavior, and promises a future better understanding of the nonlinear dynamics in our numerical simulation.

*Acknowledgments.* This work was supported by the National Science Foundation under grant number OCE-1756863. The authors are grateful for a constructive discussion on data analysis with Jonathan Lilly.

*Data availability statement.* The numerical model solution is publicly available on SciServer (http://sciserver.org), which is developed and administered by the Institute for Data Intensive Engineering and Science at Johns Hopkins University. Instructions for accessing

the data set are available at this site (https://oceanspy.readthedocs.io). The tide gauge data is available at http://uhslc.soest.hawaii.edu/network/. The Kögur array data is available at http://kogur.whoi.edu/php/index.php.

## References


Adams, J. K., and V. T. Buchwald, 1969: The generation of continental shelf waves. *Journal of Fluid Mechanics*, **35 (4)**, 815–826, doi:10.1017/S0022112069001455.

Almansi, M., R. Gelderloos, T. Haine, A. Saberi, and A. Siddiqui, 2019: OceanSpy: A Python package to facilitate ocean model data analysis and visualization. *Journal of Open Source Software*, **4 (39)**, 1506, doi:10.21105/joss.01506, URL http://joss.theoj.org/papers/10.21105/joss.01506.

Almansi, M., T. W. N. Haine, R. Gelderloos, and R. S. Pickart, 2020: Evolution of denmark strait overflow cyclones and their relationship to overflow surges. *Geophysical Research Letters*, **47 (4)**, e2019GL086 759, doi:10.1029/2019GL086759, URL https://agupubs.onlinelibrary.wiley.com/doi/abs/10.1029/2019GL086759, e2019GL086759 10.1029/2019GL086759, https://agupubs.onlinelibrary.wiley.com/doi/pdf/10.1029/2019GL086759.

Almansi, M., T. W. N. Haine, R. S. Pickart, M. G. Magaldi, R. Gelderloos, and D. Mastropole, 2017: High-Frequency Variability in the Circulation and Hydrography of the Denmark Strait Overflow from a High-Resolution Numerical Model. *Journal of Physical Oceanography*, **47 (12)**, 2999–3013, doi:10.1175/JPO-D-17-0129.1, URL http://journals.ametsoc.org/doi/10.1175/JPO-D-17-0129.1.

Bacon, S., G. Reverdin, I. G. Rigor, and H. M. Snaith, 2002: A freshwater jet on the east Greenland shelf. *Journal of Geophysical Research*, **107**, 3068, doi:10.1029/2001JC000935.

Bamber, J., M. Van Den Broeke, J. Ettema, J. Lenaerts, and E. Rignot, 2012: Recent large increases in freshwater fluxes from Greenland into the North Atlantic. *Geophysical Research Letters*, **39 (19)**, 8–11, doi:10.1029/2012GL052552.

Bras, I. A.-A. L., F. Straneo, J. Holte, and N. P. Holliday, 2018: Seasonality of Freshwater in the East Greenland Current System From 2014 to 2016. *J. Geophys. Res. Oceans*, **123**, 8828–8848, doi:10.1029/2018JC014511.

Brink, K. H., 1982: The effect of bottom friction on low-frequency coastal trapped waves. *Journal of Physical Oceanography*, **12**, 127–133, doi:10.1175/1520-0485(1982)012<0127:TEOBFO>2.0.CO;2.

Brink, K. H., 2006: Coastal-trapped waves with finite bottom friction. *Dynamics of Atmospheres and Oceans*, **41 (3-4)**, 172–190, doi:10.1016/j.dynatmoce.2006.05.001.

Brink, K. H., 2018: Stable coastal-trapped waves with stratification, topography and mean flow. https://hdl.handle.net/1912/10527.

Bromwich, D. H., and Coauthors, 2018: The arctic system reanalysis, version 2. *Bulletin of the American Meteorological Society*, **99 (4)**, 805–828, doi:10.1175/BAMS-D-16-0215.1.

Bruce, J. G., 1995: Eddies southwest of Denmark Strait. *Deep-Sea Research I*, **42**, 13–29, doi:10.1016/0967-0637(94)00040-Y.

Buchwald, V. T., and J. K. Adams, 1968: The propagation of continental shelf waves. *Proceedings of the Royal Society of London. Series A. Mathematical and Physical Sciences*, **305**, 235–250, doi:10.1098/rspa.1968.0115.

Caldwell, D. R., D. L. Cutchin, and M. S. Longuet-Higgins, 1972: Some Model Experiments on Continental Shelf Waves. *Journal of Marine Research*, **30 (1)**, 39–55.

Clarke, A. J., 1977: Observational and numerical evidence for wind-forced coastal trapped waves. *Journal of Physical Oceanography*, **7**, 231–247, doi:10.1175/1520-0485(1977)007<0231:OANEFW>2.0.CO;2.

Cummings, J. A., and O. M. Smedstad, 2013: Variational Data Assimilation for the Global Ocean. *Data Assimilation for Atmospheric, Oceanic and Hydrologic Applications (Vol. II)*, S. K. Park, and L. Xu, Eds., Springer Berlin Heidelberg, Berlin, Heidelberg, 303–343, doi:10.1007/978-3-642-35088-7{_}13, URL https://doi.org/10.1007/978-3-642-35088-7_13.

Cutchin, D. L., and R. L. Smith, 1973: Continental Shelf Waves: Low-Frequency Variations in Sea Level and Currents Over the Oregon Continental Shelf. *Journal of Physical Oceanography*, **3 (1)**, 73–82, doi:10.1175/1520-0485(1973)003<0073:cswlfv>2.0.co;2.

Dale, A. C., J. M. Huthnance, and T. J. Sherwin, 2001: Coastal-Trapped Waves and Tides at Near-Inertial Frequencies. *Journal of Physical Oceanography*, **31**, 2958–2970, doi:10.1175/1520-0485(2001)031<2958:CTWATA>2.0.CO;2.

Donlon, C. J., M. Martin, J. Stark, J. Roberts-Jones, E. Fiedler, and W. Wimmer, 2012: The Operational Sea Surface Temperature and Sea Ice Analysis (OSTIA) system. *Remote Sensing of Environment*, **116**, 140–158, doi:10.1016/j.rse.2010.10.017, URL http://dx.doi.org/10.1016/j.rse.2010.10.017.

Fischer, J., and Coauthors, 2015: Intra-seasonal variability of the DWBC in the western subpolar North Atlantic. *Progress in Oceanography*, **132**, 233–249, doi:10.1016/j.pocean.2014.04.002, URL http://dx.doi.org/10.1016/j.pocean.2014.04.002.

Foukal, N. P., R. Gelderloos, and R. S. Pickart, 2020: A continuous pathway for fresh water along the East Greenland shelf. *Science Advances*, **6 (43)**, eabc4254, doi:10.1126/sciadv.abc4254.

553 Fraser, N. J., and M. E. Inall, 2018: Influence of Barrier Wind Forcing on Heat Delivery Toward
554 the Greenland Ice Sheet. *Journal of Geophysical Research: Oceans*, **123 (4)**, 2513–2538,
555 doi:10.1002/2017JC013464.

556 Fraser, N. J., M. E. Inall, M. G. Magaldi, T. W. Haine, and S. C. Jones, 2018: Wintertime
557 Fjord-Shelf Interaction and Ice Sheet Melting in Southeast Greenland. *Journal of Geophysical*
558 *Research: Oceans*, **123 (12)**, 9156–9177, doi:10.1029/2018JC014435.

559 Gelderloos, R., T. W. N. Haine, I. M. Koszalka, and M. G. Magaldi, 2017: Seasonal Vari-
560 ability in Warm-Water Inflow toward Kangerdlugssuaq Fjord. *Journal of Physical Oceanogra-*
561 *phy*, **47 (7)**, 1685–1699, doi:10.1175/JPO-D-16-0202.1, URL http://journals.ametsoc.org/doi/
562 10.1175/JPO-D-16-0202.1.

563 Gill, A. E., and A. J. Clarke, 1974: Wind-induced upwelling, coastal currents and sea-level changes.
564 *Deep-Sea Research and Oceanographic Abstracts*, **21 (5)**, 325–345, doi:10.1016/0011-7471(74)
565 90038-2.

566 Grinsted, A., J. C. Moore, and S. Jevrejeva, 2004: Application of the cross wavelet transform
567 and wavelet coherence to geophysical time series. *Nonlinear Processes in Geophysics*, 561–566,
568 doi:10.5194/npg-11-515-2004.

569 Haine, T. W. N., 2010: High-frequency fluctuations in Denmark Strait transport. *Geophys. Res.*
570 *Lett.*, **37**, L14 601, doi:10.1029/2010GL043272.

571 Hamon, B. V., 1962: The Spectrums of Mean Sea Level at Sydney, Coff's Harbour, and Lord Howe
572 Island. *Journal of Geophysical Research*, **67 (13)**.

Hamon, B. V., 1963: Correction to 'The spectrums of mean sea level at Sydney, Coff's Harbour, and Lord Howe Island'. *Journal of Geophysical Research*, **68 (15)**, 4635–4635, doi:10.1029/jz068i015p04635.

Harden, B. E., and R. S. Pickart, 2018: High-Frequency Variability in the North Icelandic Jet. *Journal of Marine Research*, **76 (2)**, 47–62, doi:10.1357/002224018824845910.

Harden, B. E., R. S. Pickart, and I. A. Renfrew, 2014a: Offshore Transport of Dense Water from the East Greenland Shelf. *Journal of Physical Oceanography*, 229–245, doi:10.1175/JPO-D-12-0218.1.

Harden, B. E., F. Straneo, and D. A. Sutherland, 2014b: Moored observations of synoptic and seasonal variability in the East Greenland Coastal Current. *J. Geophys. Res. Oceans*, 8838–8857, doi:10.1002/2014JC010134.

Harden, B. E., and Coauthors, 2016: Upstream sources of the Denmark Strait Overflow: Observations from a high-resolution mooring array. *Deep-Sea Research Part I: Oceanographic Research Papers*, **112**, 94–112, doi:10.1016/j.dsr.2016.02.007, URL http://dx.doi.org/10.1016/j.dsr.2016.02.007.

Håvik, L., M. Almansi, K. Våge, and T. W. N. Haine, 2019: Atlantic-origin overflow Water in the East Greenland Current. *Journal of Physical Oceanography*, **49 (9)**, 2255–2269, doi:10.1175/jpo-d-18-0216.1, URL https://doi.org/10.1175/JPO-D-18-0216.1.

Håvik, L., R. S. Pickart, K. Våge, D. Torres, A. M. Thurnherr, A. Beszczynska-Möller, W. Walczowski, and W.-J. von Appen, 2017: Evolution of the East Greenland Current from Fram Strait to Denmark Strait: Synoptic measurements from summer 2012. *Journal*

*of Geophysical Research: Oceans*, **122 (3)**, 1974–1994, doi:10.1002/2016JC012228, URL https://agupubs.onlinelibrary.wiley.com/doi/abs/10.1002/2016JC012228.

Heimbach, P., D. Menemenlis, M. Losch, J. M. Campin, and C. Hill, 2010: On the formulation of sea-ice models. Part 2: Lessons from multi-year adjoint sea-ice export sensitivities through the Canadian Arctic Archipelago. *Ocean Modelling*, **33 (1-2)**, 145–158, doi:10.1016/j.ocemod.2010.02.002, URL http://dx.doi.org/10.1016/j.ocemod.2010.02.002.

Huthnance, J. M., 1978: On coastal trapped waves: Analysis and numerical calculation by inverse iteration. *Journal of Physical Oceanography*, **8**, 74–92, doi:10.1175/1520-0485(1978)008<0074:OCTWAA>2.0.CO;2.

Inall, M. E., F. Nilsen, F. R. Cottier, and R. Daae, 2015: Shelf/fjord exchange driven by coastal-trapped waves in the Arctic. *Journal of Geophysical Research: Oceans*, **120**, 8283–8303, doi:10.1002/2015JC011277.

Jackson, R. H., S. J. Lentz, and F. Straneo, 2018: The Dynamics of Shelf Forcing in Greenlandic Fjords. *Journal of Physical Oceanography*, **48 (11)**, 2799–2827, doi:10.1175/jpo-d-18-0057.1.

Jackson, R. H., F. Straneo, and D. A. Sutherland, 2014: Externally forced fluctuations in ocean temperature at Greenland glaciers in non-summer months. *Nature Geoscience*, **7 (7)**, 503–508, doi:10.1038/ngeo2186.

Jochumsen, K., M. Moritz, N. Nunes, D. Quadfasel, K. M. H. Larsen, B. Hansen, H. Valdimarsson, and S. Jonsson, 2017: Journal of Geophysical Research : Oceans. *Journal of Geophysical Research: Oceans*, **122**, 3434–3450, doi:10.1002/2017JC012803.

Johnson, E. R., and S. R. Clarke, 2001: Rossby Wave Hydraulics. *Annu. Rev. Fluid Mech.*, **33**, 207–230, doi:10.1146/annurev.fluid.33.1.207.

Katsman, C. A., S. S. Drijfhout, H. A. Dijkstra, and M. A. Spall, 2018: Sinking of dense North Atlantic waters in a global ocean model: Location and controls. *Journal of Geophysical Research: Oceans*, **123**, 3563–3576, doi:10.1029/2017JC013329.

Koszalka, I. M., T. W. N. Haine, and M. G. Magaldi, 2013: Fates and travel times of Denmark Strait overflow water in the Irminger Basin. *Journal of Physical Oceanography*, **43**, 2611–2628, doi:10.1175/JPO-D-13-023.1.

Lilly, J. M., 2019: jlab: A data analysis package for matlab, v. 1.6.6). URL http://www.jmlilly.net/software.

Losch, M., D. Menemenlis, J. M. Campin, P. Heimbach, and C. Hill, 2010: On the formulation of sea-ice models. Part 1: Effects of different solver implementations and parameterizations. *Ocean Modelling*, **33 (1-2)**, 129–144, doi:10.1016/j.ocemod.2009.12.008, URL http://dx.doi.org/10.1016/j.ocemod.2009.12.008.

Magaldi, M. G., T. W. N. Haine, and R. S. Pickart, 2011: On the nature and variability of the East Greenland Spill Jet: A case study in summer 2003. *Journal of Physical Oceanography*, **41**, 2307–2327, doi:10.1175/JPO-D-10-05004.1.

Marshall, J., A. Adcroft, C. Hill, L. Perelman, and C. Heisey, 1997: A finite-volume, incompressible Navier Stokes model for studies of the ocean on parallel computers. *Journal of Geophysical Research: Oceans*, **102 (C3)**, 5753–5766, doi:10.1029/96JC02775, URL http://doi.wiley.com/10.1029/96JC02775.

Mooers, C. N. K., and R. L. Smith, 1968: Continental shelf waves off Oregon. *Journal of Geophysical Research*, **73 (2)**, 549–557, doi:10.1029/jb073i002p00549.

637 Mysak, L. A., 1967a: On the Theory of Continental Shelf Waves. *Journal of Marine Research*,
638 **25 (3)**, 205–227.

639 Mysak, L. A., 1967b: On the very low frequency spectrum of the sea level on a continental shelf.
640 *Journal of Geophysical Research*, **72 (12)**, 3043–3047.

641 Mysak, L. A., 1980: Topographically Trapped Waves. *Annual Review of Fluid Mechanics*, **12 (1)**,
642 45–76, doi:10.1146/annurev.fl.12.010180.000401.

643 Nguyen, A. T., D. Menemenlis, and R. Kwok, 2009: Improved modeling of the arctic halocline
644 with a subgrid-scale brine rejection parameterization. *Journal of Geophysical Research: Oceans*,
645 **114 (11)**, 1–12, doi:10.1029/2008JC005121.

646 Niiler, P. P., and L. A. Mysak, 1971: Barotropic waves along an Eastern continental shelf. *Geo-*
647 *physical Fluid Dynamics*, **2**, 273–288.

648 Noël, B., W. Jan Van De Berg, H. MacHguth, S. Lhermitte, I. Howat, X. Fettweis, and M. R. Van
649 Den Broeke, 2016: A daily, 1 km resolution data set of downscaled Greenland ice sheet surface
650 mass balance (1958-2015). *Cryosphere*, **10 (5)**, 2361–2377, doi:10.5194/tc-10-2361-2016.

651 North, G. R., T. L. Bell, R. F. Cahalan, and F. J. Moeng, 1982: Sampling errors in the estimation
652 of Empirical Orthogonal Functions. *Monthly Weather Review*, **110**, 699–706, doi:10.1175/
653 1520-0493(1982)110<0699:SEITEO>2.0.CO;2.

654 Pacini, A., and Coauthors, 2020: Mean conditions and seasonality of the West Greenland
655 Boundary Current System near Cape Farewell. *Journal of Physical Oceanography*, doi:
656 10.1175/JPO-D-20-0086.1, in press.

Pawlowicz, R., B. Beardsley, and S. Lentz, 2002: Classical tidal harmonic analysis including error estimates in MATLAB using T-TIDE. *Comput. Geosci.*, **28**, 929–937, doi:10.1016/S0098-3004(02)00013-4.

Petersen, G. N., I. A. Renfrew, and G. W. K. Moore, 2009: An overview of barrier winds off southeastern Greenland during the Greenland Flow Distortion experiment. *Q. J. R. Meteorol. Soc.*, **135**, 1950–1967, doi:10.1002/qj.455.

Rhines, P., 1970: Edge-, Bottom-, and Rossby Waves in a Rotating Stratified Fluid. *Geophysical Fluid Dynamics*, **1**, 273–302.

Robinson, A. R., 1964: Continental shelf waves and the response of sea level to weather systems. *Journal of Geophysical Research*, **69 (2)**, 367–368, doi:10.1029/jz069i002p00367.

Rodney, J. T., and E. R. Johnson, 2012: Localisation of coastal trapped waves by longshore variations in bottom topography. *Continental Shelf Research*, **32**, 130–137, doi:10.1016/j.csr.2011.11.002.

Rodney, J. T., and E. R. Johnson, 2014: Meanders and Eddies from Topographic Transformation of Coastal-Trapped Waves. *Journal of Physical Oceanography*, **44**, 1133–1150, doi:10.1175/JPO-D-12-0224.1.

Rodney, J. T., and E. R. Johnson, 2015: Localised continental shelf waves: geometric effects and resonant forcing. *Journal of Fluid Mechanics*, **785**, 54–77, doi:10.1017/jfm.2015.588.

Rudels, B., E. Fahrbach, J. Meincke, G. Budeéus, and P. Eriksson, 2002: The East Greenland Current and its contribution to the Denmark Strait overflow. *ICES Journal of Marine Science*, **59**, 1133–1154, doi:10.1006/jmsc.2002.1284.

Saberi, A., T. W. N. Haine, R. Gelderloos, M. F. de Jong, H. Furey, and A. Bower, 2020: Lagrangian Perspective on the Origins of Denmark Strait Overflow. *Journal of Physical Oceanography*, **50**, 2393–2414, doi:10.1175/JPO-D-19-0210.1.

Sakov, P., F. Counillon, L. Bertino, K. A. Lister, P. R. Oke, and A. Korablev, 2012: TOPAZ4: An ocean-sea ice data assimilation system for the North Atlantic and Arctic. *Ocean Science*, **8 (4)**, 633–656, doi:10.5194/os-8-633-2012.

Spall, M. A., and J. Pedlosky, 2018: Shelf–Open Ocean Exchange Forced by Wind Jets. *Journal of Physical Oceanography*, **48**, 163–174, doi:10.1175/JPO-D-17-0161.1.

Spall, M. A., R. S. Pickart, P. Lin, W.-J. V. Appen, D. Mastropole, H. Valdimarsson, T. W. N. Haine, and M. Almansi, 2019: Frontogenesis and Variability in Denmark Strait and Its Influence on Overflow Water. *Journal of Physical Oceanography*, **49**, 1889–1904, doi:10.1175/JPO-D-19-0053.1.

Thomson, D. J., 1982: Spectrum Estimation and Harmonic Analysis. *Proceedings of the IEEE*, **70**, 1055–1096, doi:10.1109/proc.1982.12433.

Torrence, C., and G. P. Compo, 1998: A practical guide to wavelet analysis. *Bull. Amer. Meteor. Soc.*, **79**, 61–78, doi:https://doi.org/10.1175/1520-0477(1998)079<0061:APGTWA>2.0.CO;2.

von Appen, W.-J., R. S. Pickart, K. H. Brink, and T. W. N. Haine, 2014a: Water column structure and statistics of Denmark Strait overflow water cyclones. *Deep-Sea Research Part I: Oceanographic Research Papers*, **84**, 110–126, doi:10.1016/j.dsr.2013.10.007.

von Appen, W.-J., and Coauthors, 2014b: The East Greenland Spill Jet as an important component of the Atlantic Meridional Overturning Circulation. *Deep-Sea Research Part I: Oceanographic Research Papers*, **92**, 75–84, doi:10.1016/j.dsr.2014.06.002.

Wheeler, M. C., and H. H. Hendon, 2004: An All-Season Real-Time Multivariate MJO Index: Development of an Index for Monitoring and Prediction. *Monthly Weather Review*, **132**, 1917–1932, doi:10.1175/1520-0493(2004)132<1917:AARMMI>2.0.CO;2.

# LIST OF FIGURES

along the coast spanning the width of the continental shelf. There are also features propagating around Iceland and around Reykjanes Ridge. Panels (b) and (c) show the same snapshot, but zoom in to different regions, showing that slow short waves are found both along the shelf break upstream of the Denmark Strait sill (panel (b)) and on the shelf along the coast starting at the entrance of Sermilik Deep (panel (c)). Panel (b) and its inset show two phases of the phase-locking of counter-propagating waves in Denmark Strait (one travels south to north around Iceland and the other travels north to south on the Greenland side). The wavelength is roughly the length of the Denmark Strait and the waves accelerate passing through the Strait (see also Fig. 11a and the supplementary animations to verify the phase-locking). (d-f) 5–18 days. Panel (d) shows the fast shelf wave—here occupying the entire length of the model shelf. Panels (e) and (f) show the slower short waves along the shelf break in the same regions as panels (b) and (c). . . . . 43

**Fig. 8.** Variance ellipses of velocity fluctuations at (a) the 200-m isobath stations and (b) the 450-m isobath stations, color-coded by depth (m). The white circle in panel (b) is for scale, with a diameter of 20 cm $s^{-1}$. . . . . 44

**Fig. 9.** Rotary spectra of the velocity fluctuations at 100 m depth at station 4 along the 200-m isobath (solid) and station 4 along the 450-m isobath (dashed). Gray curves: cyclonic; black curves: anticyclonic. The color-coded whiskers are the frequency ranges from Fig. 4. The vertical dashed gray line is the inertial frequency 68 °N. . . . . 45

**Fig. 10.** Hovmöller diagrams of bandpass filtered SSH anomaly signals along the 200 m isoabath (green curve in Fig. 1). The along-isobath locations of the 11 stations is indicated by the black downward facing triagles. Y-axes are time (tickmarks in panel b are on the 1st of the month). Green slanted lines indicate inferred phase speeds. (a) 1-3 day pass band. (b) 5-18 day pass band. . . . . 46

**Fig. 11.** As Fig. 10 but for the 450 m isobath (magenta curve in Fig. 1). . . . . 47

**Fig. 12.** (a) Dispersion diagram for waves at cyan shelf section in Fig. 1. Red curves are for summer stratification, blue for winter. The line styles indicate the strength of the background flow with a maximum southwards surface speed of 0.1 m $s^{-1}$ (dash-dotted), 0.2 m $s^{-1}$ (dashed), 0.3 m $s^{-1}$ (solid), and 0.4 m $s^{-1}$ (dotted). The gray dashed curve is an hypothesized Mode III curve (see text). The connected open circles indicate $\omega$–$k$ combinations of waves diagnosed from the model fields (the frequency range is based on the pass-band applied in the filter; the wave number uncertainty range indicated represents half a wavelength). The insets (labeled A-D) are examples of surface structures from the Brink (1982, 2006) model solution found for the four points indicated in the diagram by solid circles. In the insets as well as panels c-e, blue is pressure, red is along-shore velocity in the direction of wave propagation, and green is cross-shore velocity away from the coast. The dashed vertical line is the position of the shelfbreak; the horizontal dotted line is the zero position on the y-axis. (b) Section bathymetry in the numerical model (black) and idealized approximation (brown). (c-e) EOF modes from an MEOF analysis on SSH anomaly, along-shore and cross-shore velocity along the cyan section in Fig. 1. (c) Mode III, explains 14% of the total variance; (d) Mode IV, explains 9% of the total variance; (e) Mode V, explains 6% of the total variance. . . . . 48

**Fig. 13.** Example of results of multivariate EOF analysis. The MEOF is performed on the 5–18 day bandpass filtered SSH anomaly and wind speed fields. (a) Second EOF for SSH from MEOF; (b) Second EOF for wind speed from MEOF; (c) Third EOF from regular EOF analysis based on wind speed only; (d) Blue: absolute value of the second principal component from the MEOF; Red dashed: 5-day low-pass filtered version of the blue curve; Green: 5–18 days band-averaged wavelet energy (see Fig. 6) at the fifth station along the 200 m isobath (green

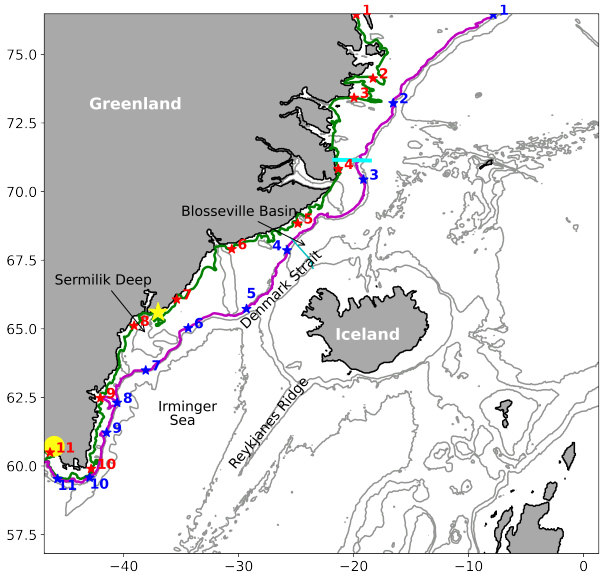


FIG. 1. Map of study region. Landmasses are gray. Bathymetry is contoured at 400 m, 1000 m, and 2000 m depth. The 200 m isobath along the Greenland coast is indicated in green. Note that the contour has been artificially altered to skip the fjords when interpolation near the coast inside these fjords would yield large data gaps. The magenta contour is the 450 m isobath along the Greenland coast. The thick cyan line is the cross-shelf section used in Section 4d. The thin cyan line is the Kögur section (see also Fig. 2). The yellow star is the location of the Ammassalik tide gauge and the yellow solid circle is the location of the Qaqortoq tide gauge. Red and blue stars are stations along the isobaths used in the text. Geographical locations in the ocean referenced in the text are indicated in black-font text.

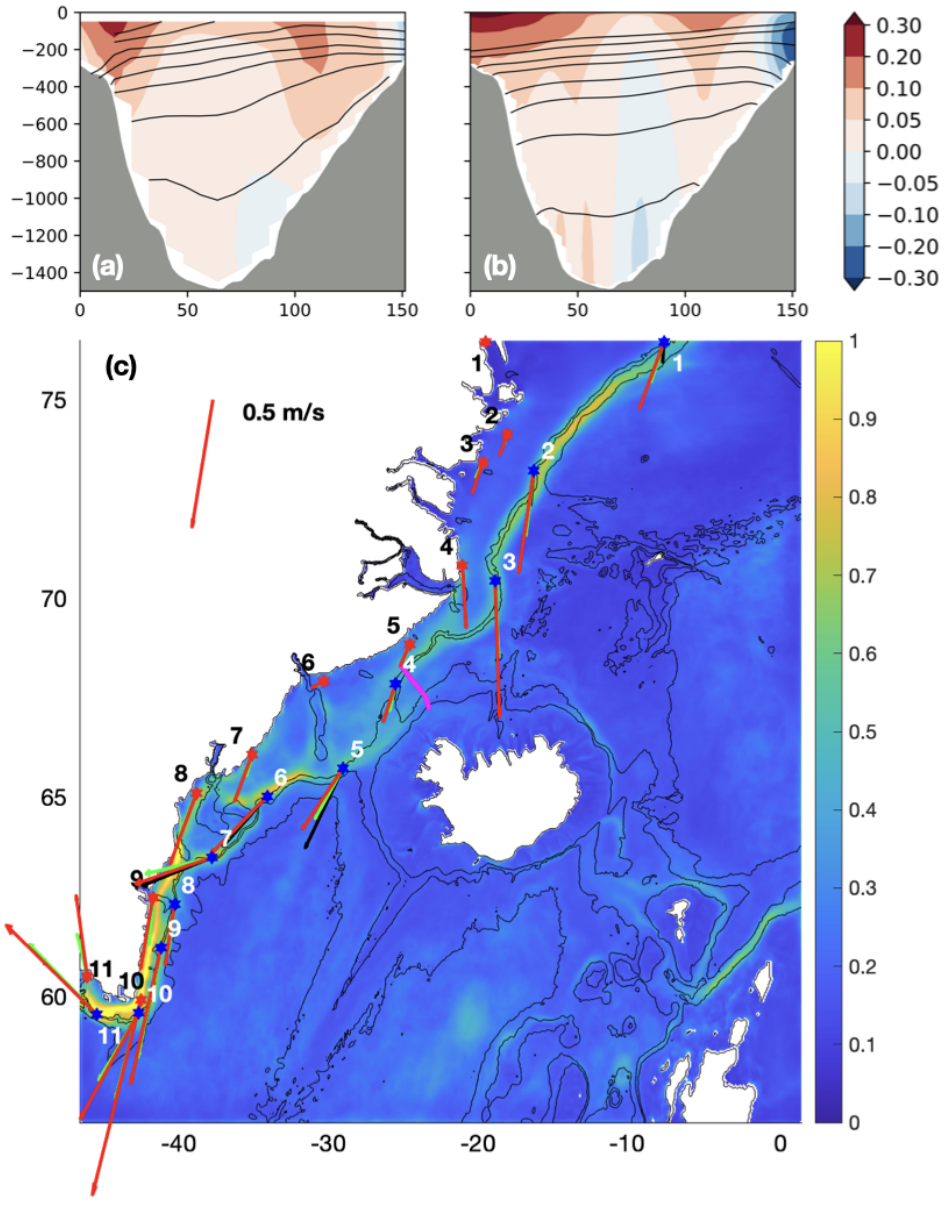


FIG. 2. Mean velocity. Panels (a) and (b) show the annual mean velocity orthogonal to the Kögur section (magenta line in panel (c)) from (a) *in situ* observations in 2011-2012 (Harden et al. 2016), and (b) the model mean from 2007-2008; positive values (m $s^{-1}$) are toward to Equator. Contoured in gray is potential density (contour levels are 27.3, 27.5, 27.7, 27.8, 27.9, 27.95, 28.0, and 28.05 kg $m^{-3}$). (c) Mean surface current speed (filled contours, in m $s^{-1}$) and mean current vectors as a function of depth (red arrows: top 50 m; green arrows: 50-200 m average; black arrows: > 200 m average) at the shelf (red stars, black numbers) and shelf break (blue stars, white numbers) stations (see also Fig. 1). The 450, 1000, and 2000 m isobath are contoured in black in panel (c).

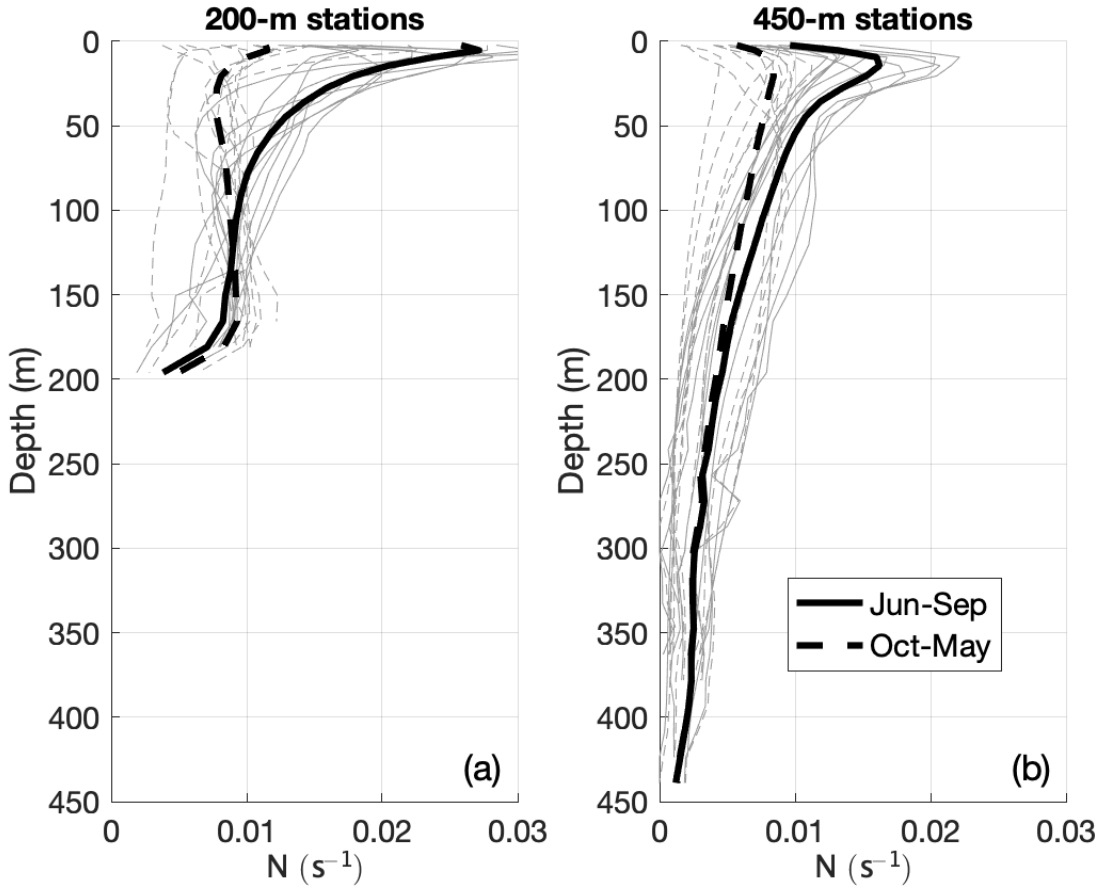


816 FIG. 3. Vertical density stratification quantified with the buoyancy frequency ($N$). Solid lines are summer
817 profiles (June–September); dashed lines are winter profiles (October–May). The gray profiles are individual
818 stations, while the thick profiles are averages over all 11 stations along the (a) 200-m isobath and (b) 450-m
819 isobath.

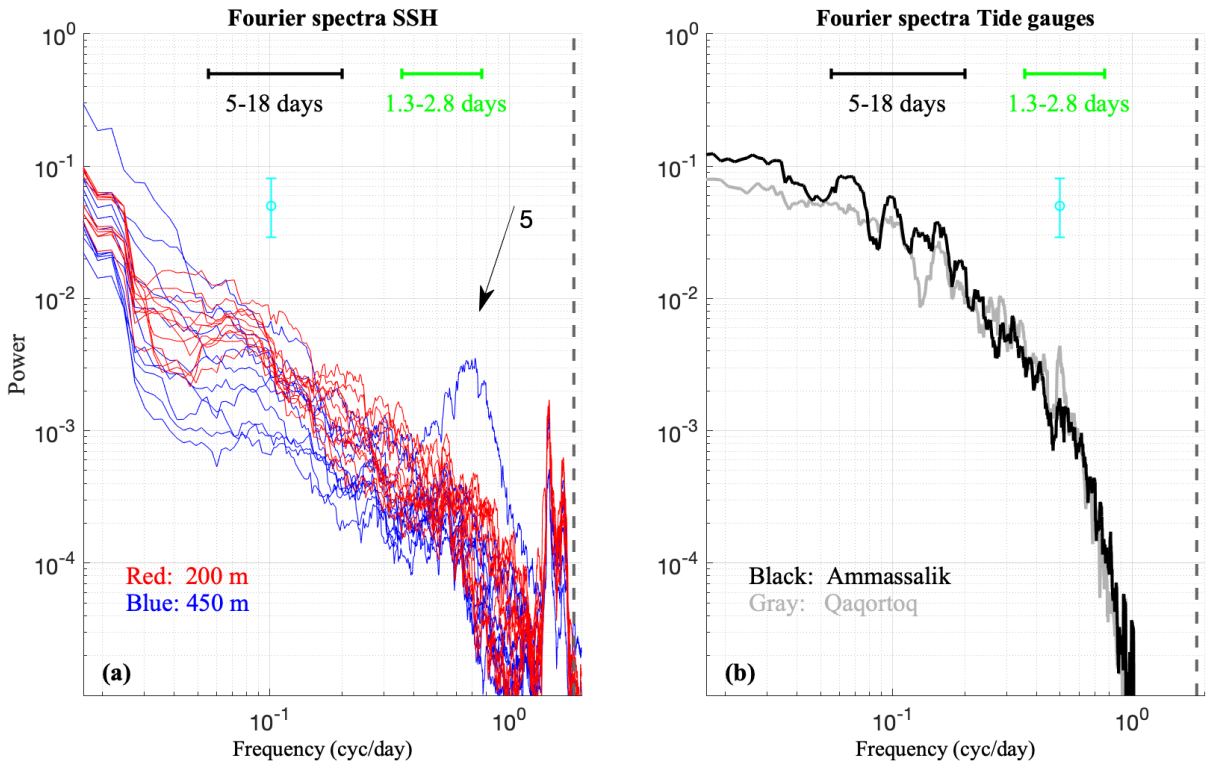


820 FIG. 4. Fourier frequency spectrum estimates for SSH. (a) Spectra for SSH anomalies at 11 stations along the
821 200-m isobath (red lines, red stars in Fig. 1) and 11 stations along the 450-m isobath (blue lines, blue stars in Fig.
822 1). The curve labeled "5" corresponds to station 5 on the 450 m isobath, i.e., the station just downstream of the
823 Denmark Strait sill. The gray vertical dashed line indicates the inertial frequency at 68°N. The horizontal bars
824 are 2 frequency ranges, annotated in days. The vertical cyan bar indicates 95% confidence limits. (b) Spectral
825 estimates from tide gauges at Ammassalik (black dashed curve) and Qaqortoq (gray dashed line). See Fig. 1 for
826 the locations of these tide gauges.

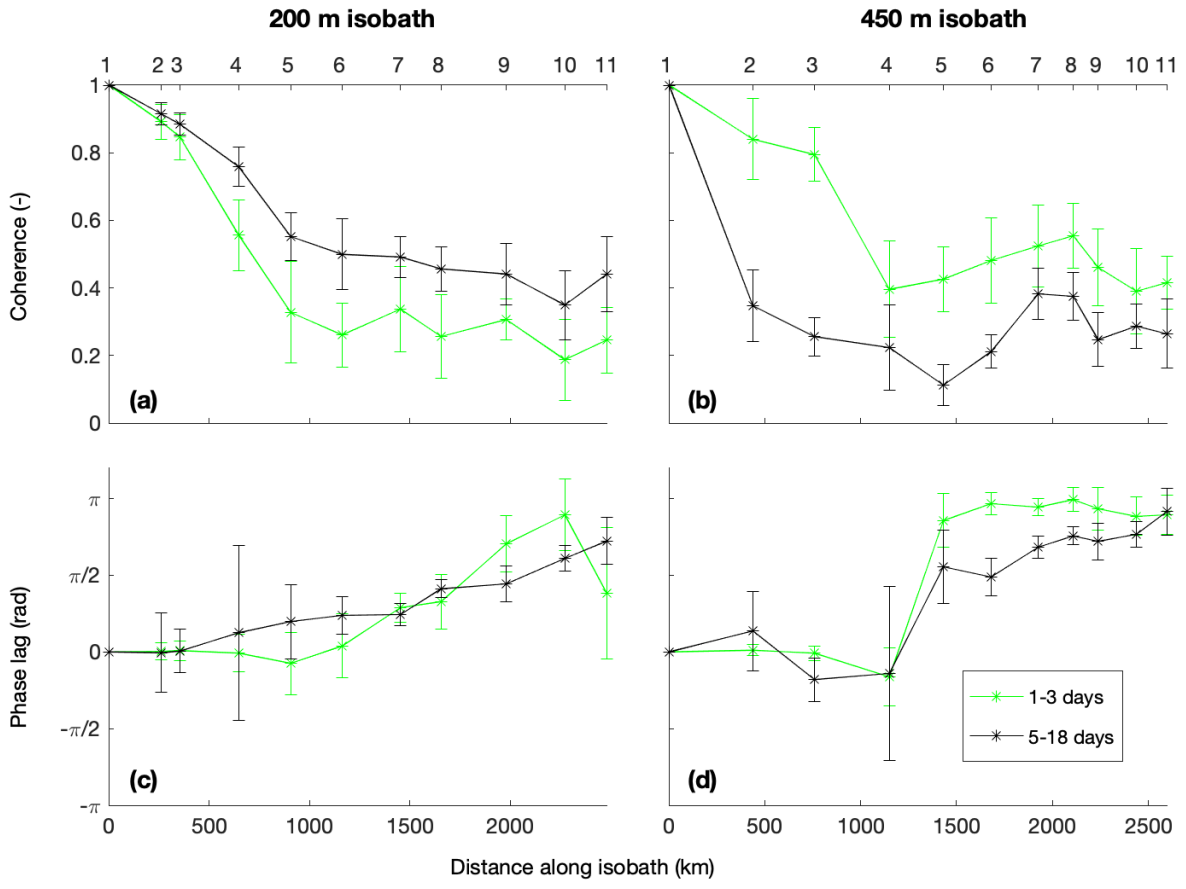


827 FIG. 5. Coherence $\gamma$ (Eq. 1) magnitude (a,b) and phase lag (c,d) between the SSH anomaly time series at
828 station 1 and the other stations along the (a,c) 200-m isobath and the (b,d) 450-m isobath (station positions are
829 indicated along the top axes). The error bars in (a,b) are the standard deviation calculated based on the frequency
830 range; the error bars in (c,d) indicate the circular standard deviation calculated over the same frequency ranges
831 (Grinsted et al. 2004). Color coding as in Fig. 4.

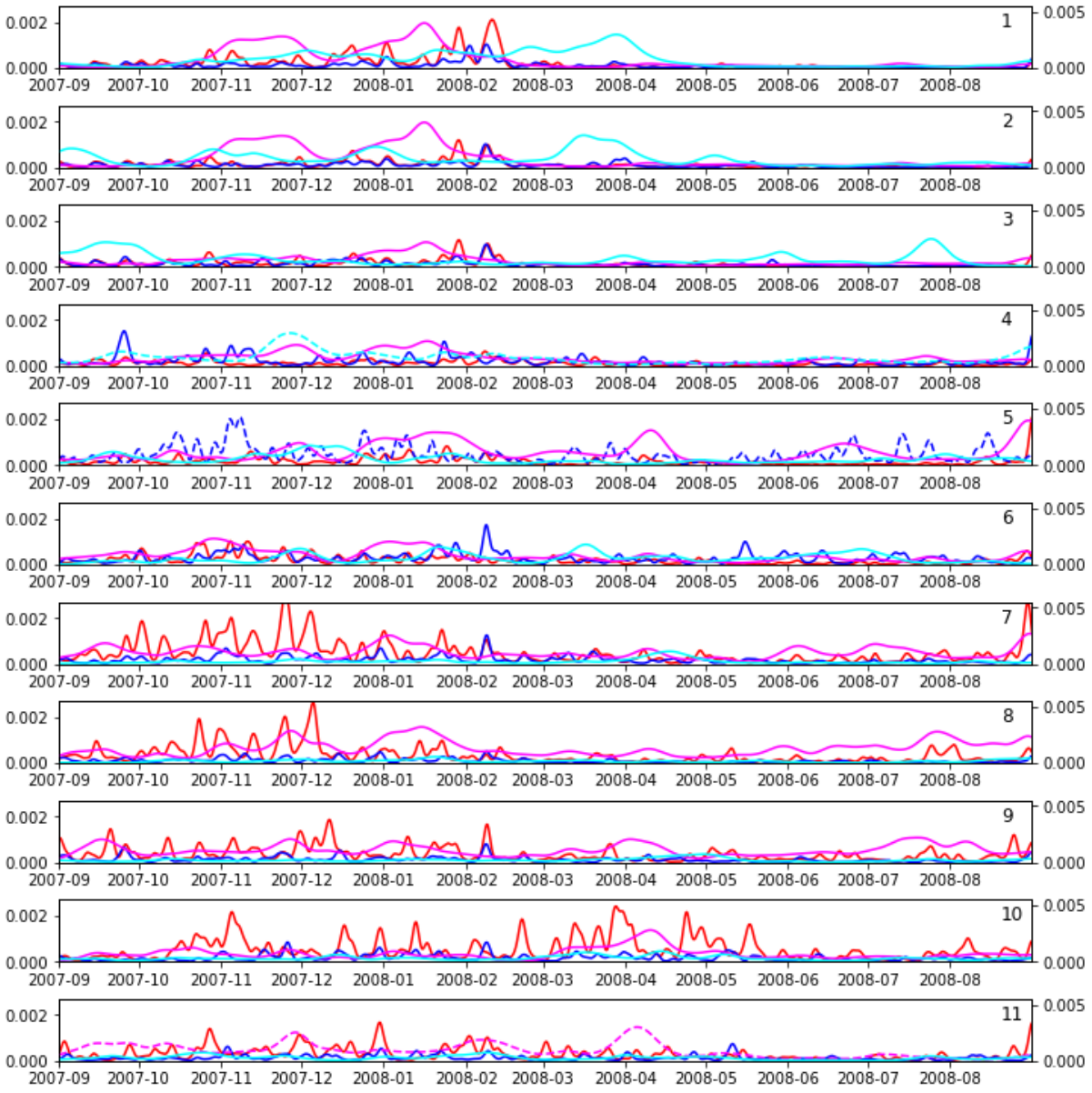


832 FIG. 6. Band-averaged wavelet energy time series for the 11 stations along the 200 m isobath and 11 stations
833 along the 450 m isobath in Fig. 1 (station numbers are in the top right corner of each panel). Red: 200 m isobath
834 stations, 1–3 days; Blue: 450 m isobath stations, 1–3 days; Magenta: 200 m isobath stations, 5–18 days; Cyan:
835 450 m isobath stations, 5–18 days. The dashed curves are scaled for visualization purposes (they would not fit
836 on the graph otherwise). For the full signal use the following multiplication factors: Blue curve at station 5: ×3;
837 Cyan curve at station 4 and magenta curve at station 11: ×2.

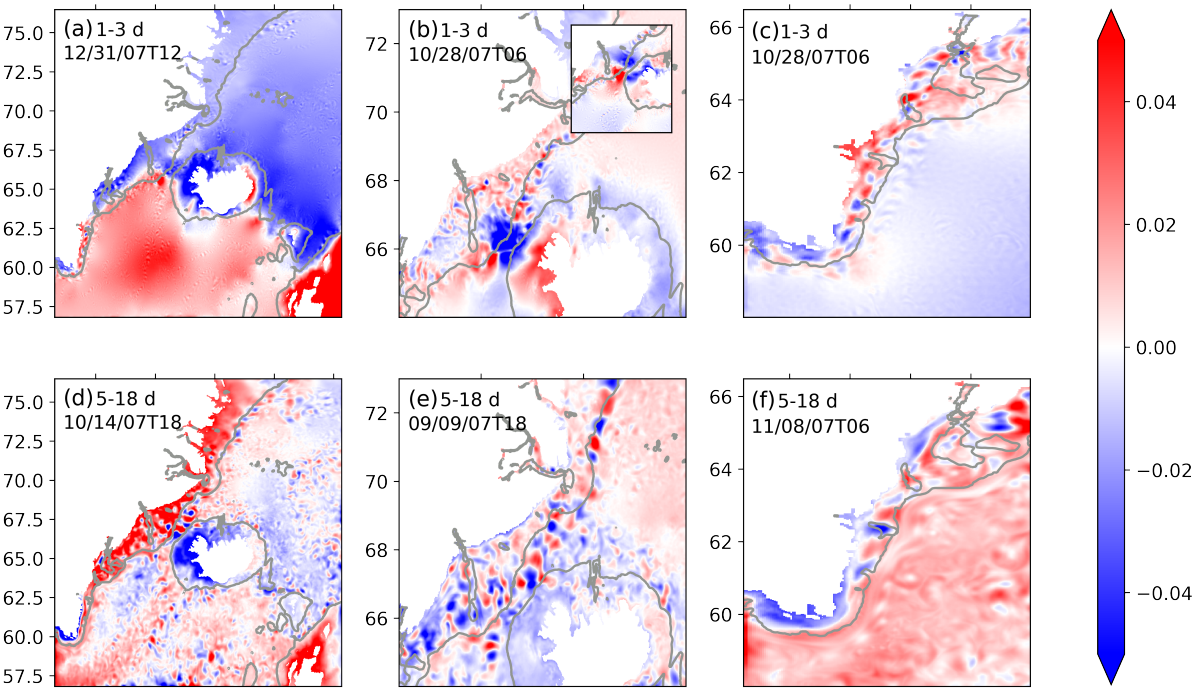


FIG. 7. Snapshots of band-passed filtered sea surface height anomalies. The snapshots are subjectively selected to highlight certain features. (a-c) 1–3 days. Panel (a) shows a shelf wave along the coast spanning the width of the continental shelf. There are also features propagating around Iceland and around Reykjanes Ridge. Panels (b) and (c) show the same snapshot, but zoom in to different regions, showing that slow short waves are found both along the shelf break upstream of the Denmark Strait sill (panel (b)) and on the shelf along the coast starting at the entrance of Sermilik Deep (panel (c)). Panel (b) and its inset show two phases of the phase-locking of counter-propagating waves in Denmark Strait (one travels south to north around Iceland and the other travels north to south on the Greenland side). The wavelength is roughly the length of the Denmark Strait and the waves accelerate passing through the Strait (see also Fig. 11a and the supplementary animations to verify the phase-locking). (d-f) 5–18 days. Panel (d) shows the fast shelf wave—here occupying the entire length of the model shelf. Panels (e) and (f) show the slower short waves along the shelf break in the same regions as panels (b) and (c).

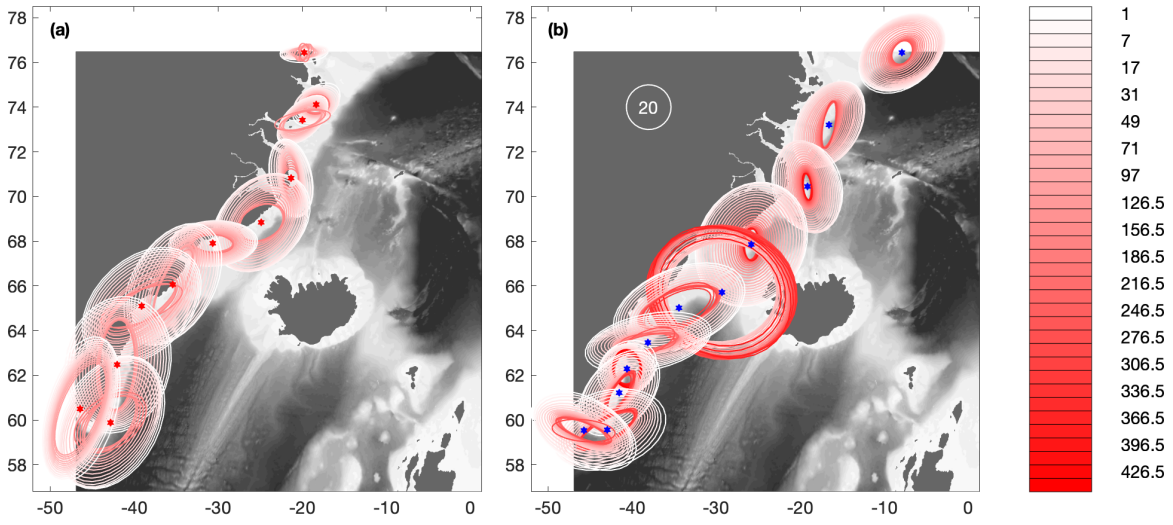


850 FIG. 8. Variance ellipses of velocity fluctuations at (a) the 200-m isobath stations and (b) the 450-m isobath
851 stations, color-coded by depth (m). The white circle in panel (b) is for scale, with a diameter of 20 cm $s^{-1}$.

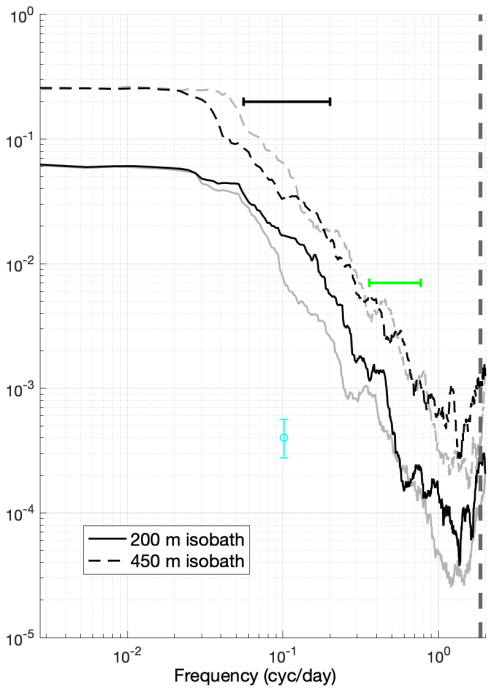


852 FIG. 9. Rotary spectra of the velocity fluctuations at 100 m depth at station 4 along the 200-m isobath (solid) and
853 station 4 along the 450-m isobath (dashed). Gray curves: cyclonic; black curves: anticyclonic. The color-coded
854 whiskers are the frequency ranges from Fig. 4. The vertical dashed gray line is the inertial frequency 68 °N.

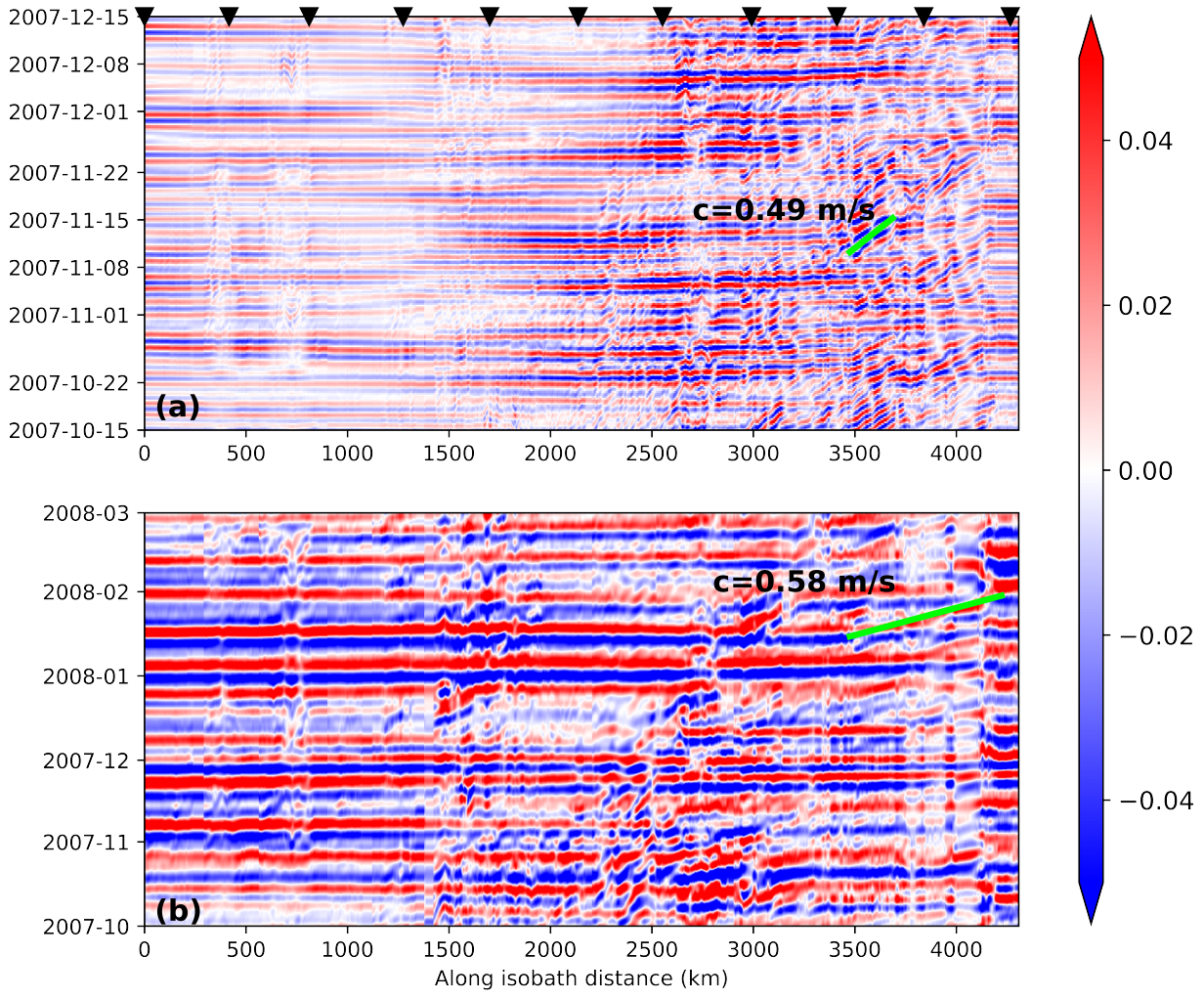


FIG. 10. Hovmöller diagrams of bandpass filtered SSH anomaly signals along the 200 m isoabath (green curve in Fig. 1). The along-isobath locations of the 11 stations is indicated by the black downward facing triagles. Y-axes are time (tickmarks in panel b are on the 1st of the month). Green slanted lines indicate inferred phase speeds. (a) 1-3 day pass band. (b) 5-18 day pass band.

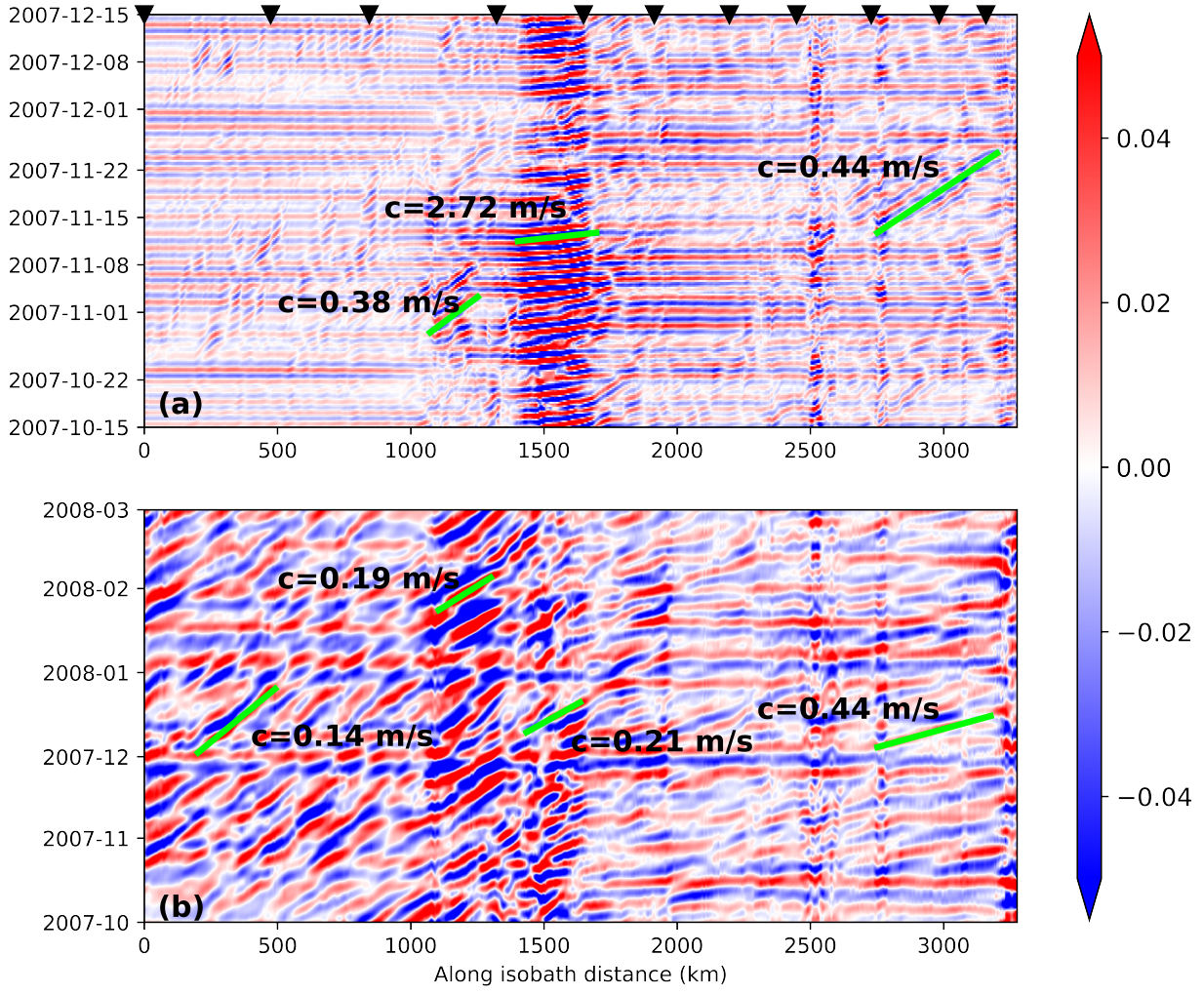


FIG. 11. As Fig. 10 but for the 450 m isobath (magenta curve in Fig. 1).

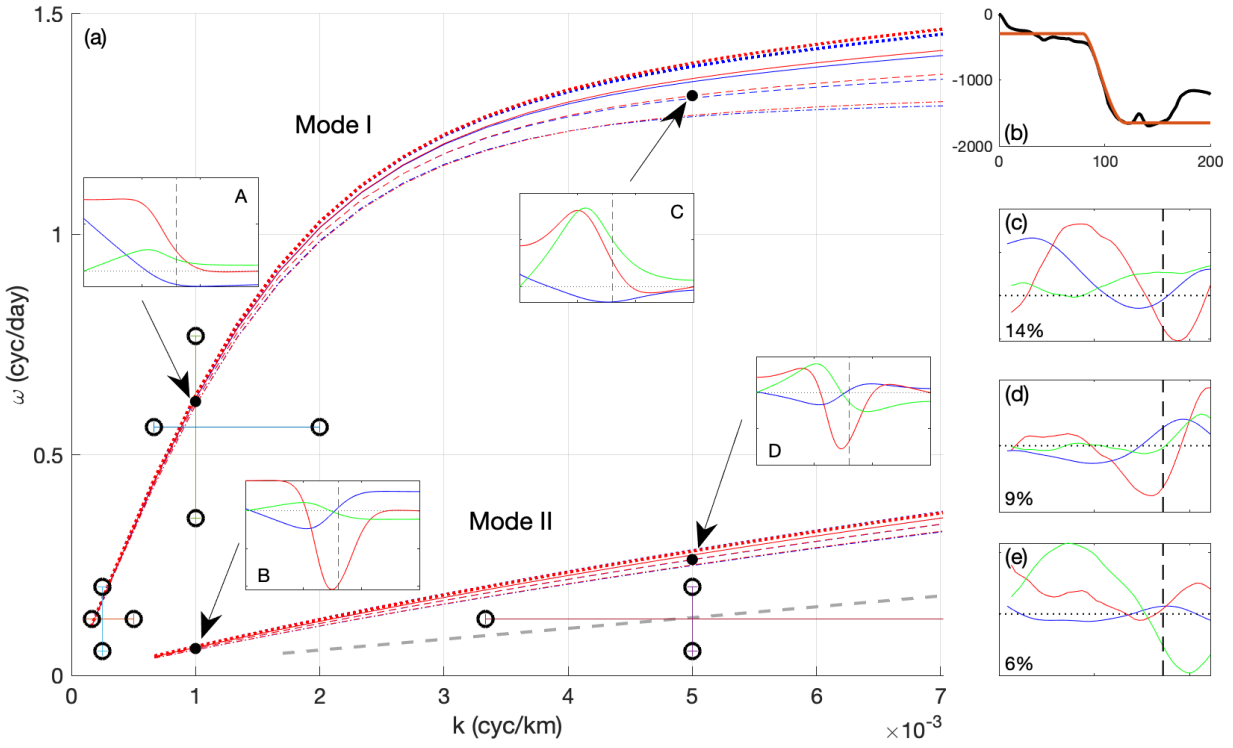


FIG. 12. (a) Dispersion diagram for waves at cyan shelf section in Fig. 1. Red curves are for summer stratification, blue for winter. The line styles indicate the strength of the background flow with a maximum southwards surface speed of 0.1 m $s^{-1}$ (dash-dotted), 0.2 m $s^{-1}$ (dashed), 0.3 m $s^{-1}$ (solid), and 0.4 m $s^{-1}$ (dotted). The gray dashed curve is an hypothesized Mode III curve (see text). The connected open circles indicate $\omega$–$k$ combinations of waves diagnosed from the model fields (the frequency range is based on the pass-band applied in the filter; the wave number uncertainty range indicated represents half a wavelength). The insets (labeled A-D) are examples of surface structures from the Brink (1982, 2006) model solution found for the four points indicated in the diagram by solid circles. In the insets as well as panels c-e, blue is pressure, red is along-shore velocity in the direction of wave propagation, and green is cross-shore velocity away from the coast. The dashed vertical line is the position of the shelfbreak; the horizontal dotted line is the zero position on the y-axis. (b) Section bathymetry in the numerical model (black) and idealized approximation (brown). (c-e) EOF modes from an MEOF analysis on SSH anomaly, along-shore and cross-shore velocity along the cyan section in Fig. 1. (c) Mode III, explains 14% of the total variance; (d) Mode IV, explains 9% of the total variance; (e) Mode V, explains 6% of the total variance.

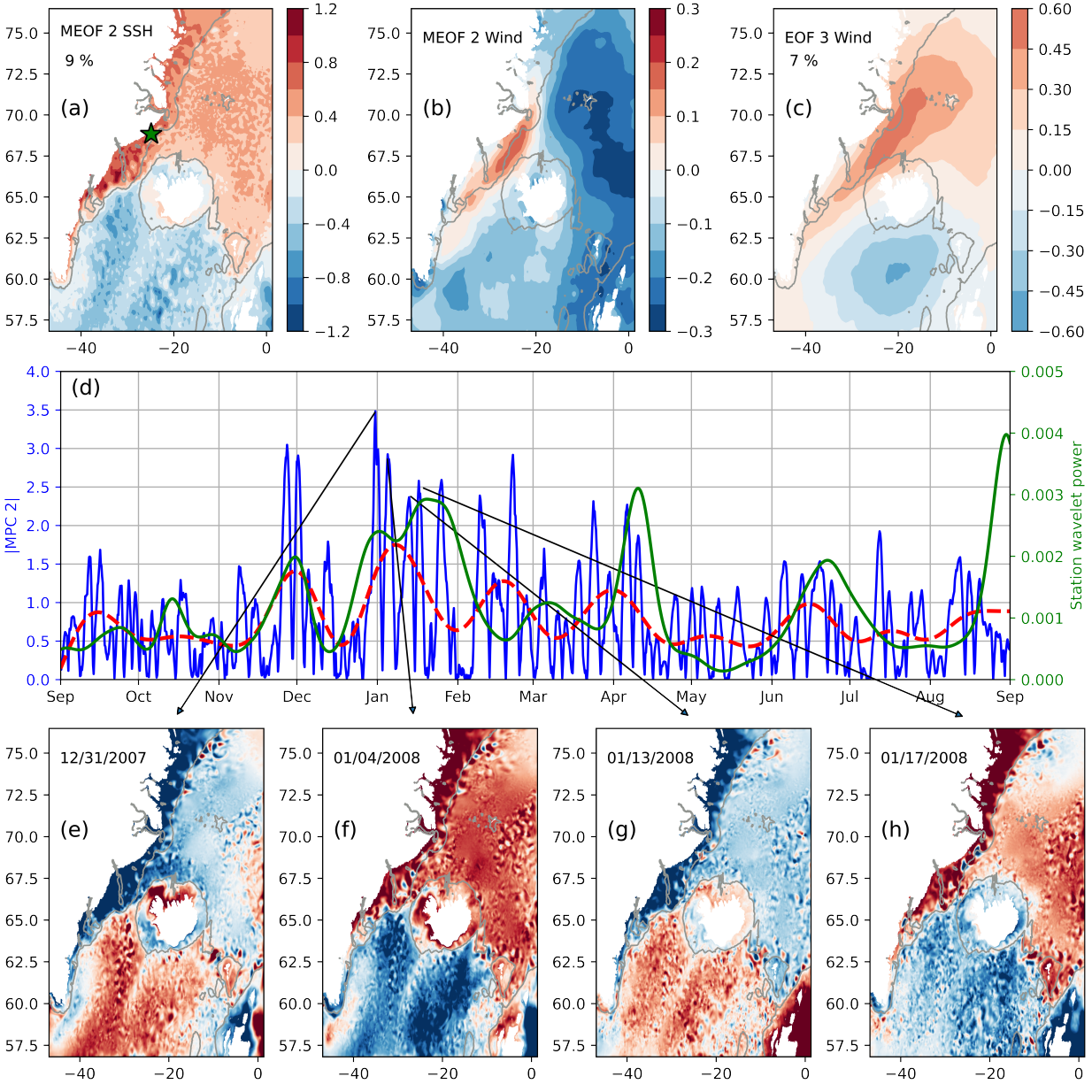


FIG. 13. Example of results of multivariate EOF analysis. The MEOF is performed on the 5–18 day bandpass filtered SSH anomaly and wind speed fields. (a) Second EOF for SSH from MEOF; (b) Second EOF for wind speed from MEOF; (c) Third EOF from regular EOF analysis based on wind speed only; (d) Blue: absolute value of the second principal component from the MEOF; Red dashed: 5-day low-pass filtered version of the blue curve; Green: 5–18 days band-averaged wavelet energy (see Fig. 6) at the fifth station along the 200 m isobath (green star in panel (a)); (e-h) Snapshots of the 5–18 day bandpass filtered SSH anomaly fields at times of maximum amplitude of the shelf wave. Times are indicated in the top left of the panels, and linked to panel (d) with gray arrows. Gray contours in panels a-c and e-h are the 450 m isobath.